

PAPER • OPEN ACCESS

Comparison between SOLPS-4.3 and the Lengyel Model for ITER baseline neon-seeded plasmas

To cite this article: D. Moulton *et al* 2021 *Nucl. Fusion* **61** 046029

View the [article online](#) for updates and enhancements.




IOP | ebooks™

Bringing together innovative digital publishing with leading authors from the global scientific community.

Start exploring the collection—download the first chapter of every title for free.

Comparison between SOLPS-4.3 and the Lengyel Model for ITER baseline neon-seeded plasmas

D. Moulton^{1,*}, P.C. Stangeby², X. Bonnin³ and R.A. Pitts³ 

¹ UKAEA-CCFE, Culham Science Centre, Abingdon, OX14 3DB, United Kingdom of Great Britain and Northern Ireland

² University of Toronto Institute for Aerospace Studies, 4925 Dufferin St, Toronto, M3H 5T6, Canada

³ ITER Organization, Route de Vinon-sur-Verdon, CS 90 046, 13067 St. Paul Lez Durance Cedex, France

E-mail: david.moulton@ukaea.uk

Received 30 July 2020, revised 5 February 2021

Accepted for publication 9 February 2021

Published 17 March 2021



Abstract

If correct, the Lengyel model offers a simple and powerful tool to predict the conditions required for detachment onset in future fusion reactors. We assess its validity against a comprehensive SOLPS-4.3 simulation database of ITER baseline ($Q = 10$) neon-seeded plasmas (Pacher *et al* 2015 *J. Nucl. Mater.* **463** 591). In absolute terms, the Lengyel Model is found to significantly overpredict the simulated impurity concentration required in the ITER outer divertor for outer target ion flux rollover (by a factor ~ 4.3 in this particular case). Importantly though, at detachment onset, and even beyond onset, the Lengyel model does give a remarkably accurate prediction of the *scaling* interdependencies between the electron density at the outer divertor entrance, the parallel energy flux density at the outer divertor entrance, and the impurity concentration in the outer divertor. However, the generalisation of these two key results to other machines, and in the presence of additional physics not included in these simulations, requires further studies. The analysis techniques described here provide a framework for such studies. Regarding the factor ~ 4.3 overprediction of the simulated outer divertor impurity concentration, the main contributors to the disagreement are found to be other energy loss mechanisms besides impurity cooling (primarily neutral losses and radial transport) combined with convective energy fluxes near the target, as well as non-constant electron static pressure due to poloidally variable T_i/T_e . None of these are included in the Lengyel model. By themselves, these do not strongly influence the scaling interdependencies of the main Lengyel parameters over the explored parameter range. The impurity residence time τ is observed to increase with density, which tends to flatten out the impurity concentration scaling at low density, relative to the Lengyel model (which usually assumes constant τ). In these simulations, however, this flattening out was cancelled by an accumulation of other effects, so that the scaling prediction of the Lengyel model was still well met. A simple physics model is derived for $n_e\tau$ that matches the simulation data well. Neon is found to migrate from the inner divertor to the outer divertor with increased puffing, thereby

* Author to whom any correspondence should be addressed.



Original content from this work may be used under the terms of the [Creative Commons Attribution 4.0 licence](https://creativecommons.org/licenses/by/4.0/). Any further distribution of this work must maintain attribution to the author(s) and the title of the work, journal citation and DOI.

increasing the outer divertor neon enrichment. At outer target ion flux rollover, though, the enrichment is approximately independent of the upstream concentration, so that the Lengyel model predicts well the scaling dependency between the upstream impurity concentration and the upstream electron density, both key quantities dictating the operational range of a tokamak.

Keywords: SOLPS, ITER, detachment, Lengyel, divertor, residence time, impurity

(Some figures may appear in colour only in the online journal)

1. Introduction

The Lengyel model [1] continues to be used in many scrape-off layer (SOL) studies in order to relate the divertor conditions (in terms of the impurity concentration in the divertor, the upstream SOL electron density, and the upstream parallel energy flux density) to the power dissipated. See e.g. [2–13]. If detachment onset is assumed to occur at the point where plasma power dissipation is total (or when the target temperature reaches a certain value), then the Lengyel model can be used to calculate the divertor conditions required for detachment onset. In this paper we assess the validity of the Lengyel model by comparing it to the SOLPS-4.3 (no drifts⁴) simulation database of ITER $Q = 10$ baseline neon-seeded plasmas, first presented in [14] and more recently in [15].

It is useful to rederive the Lengyel model, while accounting for the extra terms included in SOLPS-4.3. The total plasma energy balance equation in the code is

$$B \frac{d}{ds} \left(\frac{q_{\parallel}}{B} \right) = n_e^2 c_{\alpha} L_{\alpha}^{\text{SOLPS}} + S_{Q\text{other}}, \quad (1)$$

where

$$q_{\parallel} = \kappa_{e\parallel 0, \text{FL}} T_e^{5/2} \frac{dT_e}{ds} + q_{\parallel \text{other}}, \quad (2)$$

is the total parallel kinetic energy flux density associated with charged particle motion, B is the magnetic field strength, and s is the parallel distance along the flux tube of interest. Note that s is defined to increase away from the target, while q_{\parallel} is defined as positive towards the target.

The first term on the right-hand side of (1) is the energy loss density due to cooling by the primary impurity radiator α :

$$S_{Q\alpha} = n_e^2 c_{\alpha} L_{\alpha}^{\text{SOLPS}}, \quad (3)$$

where n_e is the electron density,

$$c_{\alpha} = \sum_{z=0}^{z_{0,\alpha}} n_{\alpha_z} / n_e, \quad (4)$$

is the concentration of impurity species α (with proton number $z_{0,\alpha}$ ⁵), z is the charge number of impurity ionisation state α_z

(with density n_{α_z}),

$$L_{\alpha}^{\text{SOLPS}} = \sum_{z=0}^{z_{0,\alpha}} F_{\alpha_z}^{\text{SOLPS}} \eta_{\alpha_z}^{\text{STRAHL}}, \quad (5)$$

is the electron cooling function from SOLPS due to the primary impurity radiator,

$$F_{\alpha_z}^{\text{SOLPS}} = n_{\alpha_z} / \sum_{z=0}^{z_{0,\alpha}} n_{\alpha_z}, \quad (6)$$

is the SOLPS-calculated fractional abundance of α_z (which includes impurity transport effects), and $\eta_{\alpha_z}^{\text{STRAHL}}$ is the electron cooling coefficient for α_z . These $\eta_{\alpha_z}^{\text{STRAHL}}$ values are inputs to SOLPS and include line radiation, recombination, bremsstrahlung and ionisation cost. For the particular simulations analysed here, they were taken from the STRAHL database [16]. Their calculation assumes a sufficiently low electron density that effects such as electron impact de-excitation can be ignored (the coronal approximation); $\eta_{\alpha_z}^{\text{STRAHL}}$ are therefore density independent⁶. In most applications of the Lengyel model, cooling by the primary impurity radiator is assumed to be the dominant energy loss mechanism. However, SOLPS includes other energy loss mechanisms due to plasma interactions with deuterium neutrals $S_{Q\text{neut}}$ and net radial energy flux out of the considered flux tube $S_{Q\text{RT}}$:

$$S_{Q\text{other}} = S_{Q\text{neut}} + S_{Q\text{RT}}. \quad (7)$$

Coming back to equation (2), the first term on the right-hand side of (2) is the electron-conducted component of q_{\parallel} :

$$q_{\parallel \text{e,cond}} = \kappa_{e\parallel 0, \text{FL}} T_e^{5/2} \frac{dT_e}{ds}, \quad (8)$$

where $\kappa_{e\parallel 0, \text{FL}}$ (units $\text{Wm}^{-1} \text{eV}^{-7/2}$) is the parallel electron heat conductivity divided by $T_e^{5/2}$ after any flux limiting procedure has been applied and T_e is the electron temperature (units eV). In most applications of the Lengyel model, electron conduction is assumed to be the dominant energy transport mechanism in the parallel direction. However, SOLPS includes other energy transport mechanisms due to electron

⁴ The importance of drifts is considered further in appendix A.

⁵ We consider only neon in this paper for which $\alpha = \text{'Ne'}$ and $z_{0,\text{Ne}} = 10$. Sputtered tungsten was not included in these simulations. Helium was included but plays a negligible role in the power balance.

⁶ It should be noted that the default option in the more recent SOLPS-ITER code is to use ADAS 96 rates for neon, which include non-coronal effects so that the electron cooling coefficients are density dependent. We emphasize that the coronal approximation used here does not imply any transport-free approximations; the transport of each impurity charge state is followed in the code.

convection $q_{||e,conv}$, ion conduction $q_{||i,cond}$ and ion convection $q_{||i,conv}$:

$$q_{||other} = q_{||e,conv} + q_{||i,cond} + q_{||i,conv}. \quad (9)$$

We now integrate equations (1) and (2) to obtain an expression for $q_{||}$ at the target end of an SOL flux tube:

$$q_{||t} = \left(q_{||u}^2 - 2 \int_t^u \kappa_{e||0,FL} T_e^{5/2} n_e^2 c_\alpha L_\alpha^{SOLPS} dT_e + 2t_B - 2t_{other} \right)^{1/2}, \quad (10)$$

where u and t in the integral limits refer respectively to the divertor entrance ('u' for 'upstream') and to the target. The term

$$t_B = \int_t^u B q_{||} d \left(\frac{q_{||}}{B} \right) - \int_t^u q_{||} dq_{||}, \quad (11)$$

accounts for variation in the magnetic field strength along the divertor leg (typically small for conventional divertors like ITER's); $t_B = 0$ when B is constant. The term

$$t_{other} = \int_t^u B q_{||other} d \left(\frac{q_{||}}{B} \right) + \int_t^u \kappa_{e||0,FL} T_e^{5/2} S_{Qother} dT_e, \quad (12)$$

accounts for the effect of other heat flux mechanisms besides electron conduction, as well as other heat loss mechanisms besides neon cooling. This term will be considered further in section 4.2.

Equation (10) is the SOLPS-4.3 equivalent of the self-contained Lengyel model discussed below. Note that it is not an alternative to the Lengyel model because it requires inputs from the SOLPS-4.3 simulations. Nevertheless, its equivalent form to the Lengyel model means that we can use (10) to better understand discrepancies between the simulations and the Lengyel model. This analysis will be presented in section 4.1.

Now, in order to move from equation (10) to a self-contained set of solvable equations, we assume that:

- (a) The electron static pressure $n_e T_e$ is constant in the region of impurity cooling, but drops to half its upstream value in a target-localised region such that the total (static plus dynamic) pressure is conserved. In addition, c_α , $\kappa_{e||0,FL}$, and B are assumed constant along the flux tube of interest.
- (b) L_α^{SOLPS} can be accurately represented by

$$L_\alpha^{n_e \tau}(T_e) = \sum_{z=0}^{z_{0,\alpha}} F_{\alpha z}^{n_e \tau} \eta_{\alpha z}^{STRAHL}. \quad (13)$$

Here, in order to approximate the impurity transport, the fractional abundances $F_{\alpha z}^{n_e \tau}(T_e)$ are taken from an ionisation balance calculation for a population of impurity atoms exposed to a plasma at fixed n_e and T_e for a 'residence' time τ [17].

- (c) $q_{||other} = S_{Qother} = 0$.
- (d) The ion and electron target temperatures are equal $T_{it} = T_{et}$.

These assumptions, in addition to a sheath heat transmission boundary condition and a specification of the connection

length, give the following three equations:

$$q_{||t} = \left(q_{||u}^2 - 2 \kappa_{e||0,FL} c_\alpha n_{eu}^2 T_{eu}^2 \int_t^u L_\alpha^{n_e \tau}(T_e) \sqrt{T_e} dT_e \right)^{1/2}, \quad (14)$$

$$q_{||t} = \gamma (n_{eu} T_{eu} / 2) \sqrt{2 T_{et} / m_i} \quad (15)$$

$$L_{||} = \kappa_{e||0,FL} \int_t^u T_e^{5/2} / q_{||}(T_e) dT_e, \quad (16)$$

where γ is the sheath energy transmission coefficient. Equations (14)–(16) are the equations previously solved in [12] and will henceforth be referred to as the 'full' Lengyel model, after the author who first introduced equation (14) [1].

In order to predict the detachment onset, the full Lengyel model can be solved with assumptions for γ and the T_{et} at which detachment occurs. Alternatively, equations (14)–(16) can be simplified further, by assuming $q_{||t} = T_{et} = 0$ and the standard two-point model expression for T_{eu} [18]. This 'simplified' Lengyel model is then a direct expression that can be rearranged for c_α , $q_{||u}$ or n_{eu} :

$$c_\alpha = \frac{q_{||u}^2}{2 \kappa_{e||0,FL} n_{eu}^2 (T_{eu}^{2PM})^2 \int_0^{T_{eu}^{2PM}} L_\alpha^{n_e \tau} \sqrt{T_e} dT_e}, \quad (17)$$

with

$$T_{eu}^{2PM} = \left(\frac{7}{2} \frac{q_{||u} L_{||}}{\kappa_{e||0,FL}} \right)^{\frac{2}{7}}. \quad (18)$$

In this paper we will compare to both the full and simplified Lengyel models.

The Lengyel model is potentially very useful for predicting the point in $(c_\alpha, q_{||u}, n_{eu})$ -space at which a future machine will detach. The purpose of this paper is to gauge its validity, by comparing it (with the help of equation (10)) to SOLPS-4.3 solutions for the ITER divertor.

The paper is organised as follows. In section 2, details are presented of how we compared the simulations to the Lengyel models, in particular what simulation outputs were used as inputs to (and compared to outputs of) the Lengyel models. Section 3 shows the comparison itself. Section 4 provides an in depth analysis of the comparison, giving the reasons for the differences between the simulations and the Lengyel model predictions. Section 5 looks at the validity of using a fixed $n_e \tau$ approximation to the neon transport in the Lengyel model, and describes a novel predictive model for $n_e \tau$ which fits the simulated data well. In section 6 we investigate the important topic of neon enrichment, which is not accounted for by the Lengyel model. Finally, in section 7 we draw our conclusions.

2. Detailed methodology behind the comparison to the Lengyel model

2.1. The SOLPS-4.3 database

We will compare the Lengyel model to the SOLPS-4.3 simulation database of $Q = 10$ baseline neon-seeded plasmas previously presented in [14]. In this database, nine puff scans

Table 1. The nine puff scans within the database assessed here, as first presented in [14]. Each tick represents a scan containing between 5 and 10 converged simulations.

	Input power P_{in} (MW)			
	60	80	100	120
0.3			✓	
0.4	✓	✓	✓	✓
0.6			✓	
0.8			✓	
1.2			✓	
$\langle c_{\text{Ne}} \rangle_{\text{sep}}$ (%)			✓	

were carried out, constituting 72 converged simulations in total. By ‘puff scan’ here we mean that *both* the D_2 puffing rate *and* the neon puffing rate were varied such that the separatrix neon concentration, $\langle c_{\text{Ne}} \rangle_{\text{sep}}$, was kept fixed. Here, $\langle c_{\text{Ne}} \rangle_{\text{sep}}$ is defined as the total number of neon particles (all charge states including neutral neon) divided by the total number of electrons, in the portion of the first SOL flux ring that lies above the x-point⁷. We assume this to be an ‘operationally relevant’ parameter, in the sense that it affects the core impurity concentration and thereby the operational range of the tokamak. Six of the nine puff scans were performed at input power $P_{\text{in}} = 100$ MW, $\langle c_{\text{Ne}} \rangle_{\text{sep}} = \{0.3, 0.4, 0.6, 0.8, 1.2, 1.8\}$ %, while the other three were done at $P_{\text{in}} = \{60, 80, 120\}$ MW, $\langle c_{\text{Ne}} \rangle_{\text{sep}} = 0.4\%$ (see table 1). For all simulations, the D^+ particle flux across the core boundary was fixed at $9.1 \times 10^{21} \text{ s}^{-1}$. This mimics pellet and NBI fuelling (the latter being much less significant on ITER). See [14, 15] for more details of the simulation setup. A list of all the simulation IDS case numbers can be found in [19]; all simulations are available in the public ITER IMAS database.

2.2. The third SOL flux ring is chosen for analysis

Within this database, we focus our assessment of the Lengyel model on the operationally-limiting flux ring in the outer divertor, from a target loading standpoint. This is defined as the last flux ring whose total target heat load drops below 16 MWm^{-2} as the puffing is increased (note that, as the puffing increases, the location of the maximum target heat load moves radially outwards). We choose 16 MWm^{-2} as an approximate maximum tolerable stationary heat load, on the basis of the new analysis presented by [15]. Our focus is on the outer divertor, rather than the inner, because the maximum target heat load usually occurs here (except at the very highest puff rates, beyond outer target flux rollover, when the maximum inner target load can slightly exceed the maximum outer target load; see figure 13 of [15]).

Figures 1(a) and (b) show near-SOL zoom-ins on the total outer target heat load profiles mapped to the outer mid-plane, including contributions from charged particles (kinetic energy and surface recombination to atoms), neutrals (kinetic energy and surface recombination to molecules) and photons. As in

[15], the charged particle contribution is multiplied by a factor $\sin(4.2^\circ) / \sin(2.7^\circ)$ to account for tile shaping⁸. For each puff scan, profiles are shown for the highest puff case at which the maximum total target load still exceeds 16 MWm^{-2} .⁹ Also shown in figures 1(a) and (b) are the reductions in the total target heat load due to anomalous net radial energy transport out of each flux ring (positive values cause a decrease in the load).

An important conclusion from these plots is that the first SOL flux ring is not operationally-limiting, because of the large radial flow of energy into the PFR (assuming diffusive anomalous radial transport; for these simulations values of $D_{\perp} = 0.3 \text{ m}^2\text{s}^{-1}$ and $\chi_{\perp} = 1 \text{ m}^2\text{s}^{-1}$ were kept constant over the whole grid). This is fortunate from the point of view of the Lengyel model, which does not account for radial transport. The second and third SOL flux rings can be regarded as equally operationally-limiting in that, for all puff scans, the last flux ring to drop below a target load of 16 MWm^{-2} is always the second or third SOL ring. However, we choose to compare the Lengyel model to the third SOL ring here because of the much lower net radial transport sink on that ring. The outer divertor portion of this flux ring is highlighted in magenta in figure 1(c). Note that this ring sits at a distance $\sim \lambda_q$ from the separatrix, calculated in the same way as described in [15].

2.3. Simulated quantities used for the Lengyel model comparisons

Having chosen our flux ring of interest, we now describe the simulated quantities that were used for the Lengyel model comparisons. The key quantities in the Lengyel models are the upstream parallel energy flux density $q_{\parallel\text{u}}$, the impurity concentration c_{Ne} , and the upstream electron density n_{eu} . We begin by discussing these.

2.3.1. $q_{\parallel\text{u}}$. In all cases, $q_{\parallel\text{u}}$ was taken at the outer divertor entrance of SOL ring 3. In the constant P_{in} , variable $\langle c_{\text{Ne}} \rangle_{\text{sep}}$ simulations (vertical ticks in table 1), the simulated $q_{\parallel\text{u}}$ values were held approximately constant and used as inputs to the Lengyel models. These inputs are given in figure 2(a) using a legend convention that will be repeated throughout the paper: values before, at, and after outer target ion flux rollover in ring 3 are plotted as dots, diamonds and open circles, respectively. As expected in the absence of drifts and current, the $q_{\parallel\text{u}}$ is approximately constant at constant P_{in} . Meanwhile, in the constant $\langle c_{\text{Ne}} \rangle_{\text{sep}}$, variable P_{in} simulations (horizontal ticks in table 1), the simulated $q_{\parallel\text{u}}$ varied significantly and was compared to the output of the Lengyel models. Since in these simulations $q_{\parallel\text{u}}$ was regarded as an output of the Lengyel models rather than an input, we do not

⁸ Without tile shaping, the angle between the magnetic field and the toroidally symmetric target surface is 2.7° . However, with toroidal tile shaping (necessary to avoid exposed leading edges), the average angle between the magnetic field and the toroidally asymmetric target surface has an increased value of 4.2° . To account for this, we multiply the toroidally symmetric simulated target heat loads by a factor $\sin(4.2^\circ) / \sin(2.7^\circ)$.

⁹ Note that, for the $\{P_{\text{in}} = 60 \text{ MW}, \langle c_{\text{Ne}} \rangle_{\text{sep}} = 0.4\%\}$ puff scan, there are no simulations for which the maximum load lies above 16 MWm^{-2} , so we show the lowest puff case.

⁷ A flux ring is the volume enclosed by two adjacent flux surfaces on the numerical grid, and by the two targets.

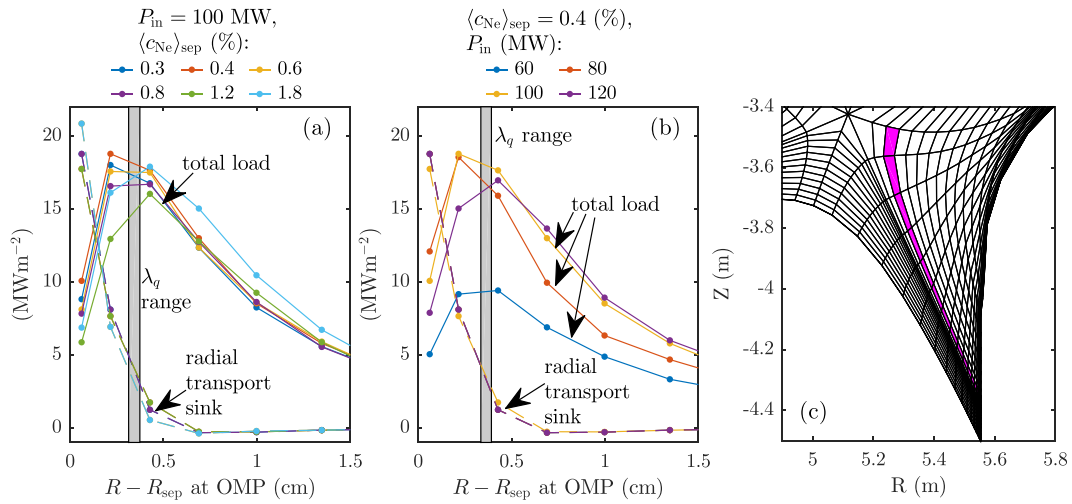


Figure 1. Justification for focussing our analysis on the third SOL flux ring. The total outer target heat load profiles (including neutral, plasma and radiation contributions) are shown for the maximum puff simulation before the peak heat load drops below 16 MWm^{-2} . Each point corresponds to a single flux ring. Note that all profiles are zoomed in and mapped to the outer mid-plane; PFR values are not plotted. The reduction in the total load due to net radial transport out of each flux ring is also shown (positive values cause a decrease in target heat load). The λ_q range is also indicated by a shaded band, calculated in the same way as in [15]. In all cases, λ_q is the distance from zero to some point inside the grey band. (a) For constant $P_{in} = 100 \text{ MW}$ and variable $\langle c_{Ne} \rangle_{sep}$ (as labelled). (b) For constant $\langle c_{Ne} \rangle_{sep} = 0.4\%$ and variable P_{in} (as labelled). (c) The numerical grid with the outer divertor portion of the third SOL flux ring highlighted in magenta (note that we show only the outer ring here; the entire ring runs between the two targets).

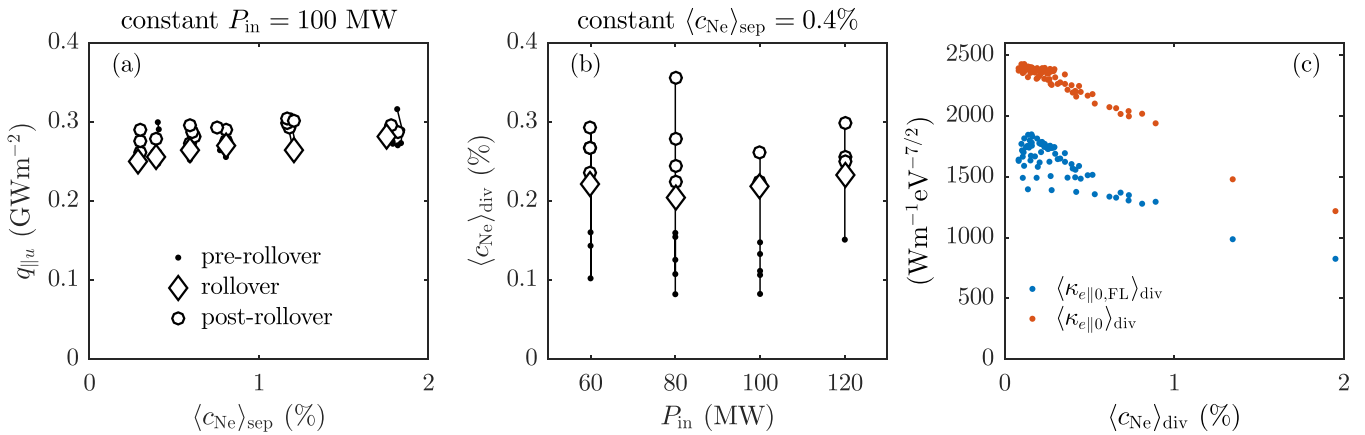


Figure 2. Some of the inputs to the Lengyel model. (a) $q_{||u}$ at the outer divertor entrance for the third SOL ring as a function of $\langle c_{Ne} \rangle_{sep}$, for the puff scans in the third column of table 1 (constant $P_{in} = 100 \text{ MW}$, variable $\langle c_{Ne} \rangle_{sep}$). (b) $\langle c_{Ne} \rangle_{div}$ in the third SOL ring as a function of P_{in} for the puff scans in the second row of table 1 (constant $\langle c_{Ne} \rangle_{sep} = 0.4\%$, variable P_{in}). Values in (a) and (b) are shown before, at, and after rollover of the outer target particle flux for SOL ring 3. (c) Parallel-averaged $\kappa_{e||0}$ for the third SOL ring in the outer divertor for all of the simulations in the database. Flux-limited and non-flux-limited values are given.

plot it in figure 2; the simulated $q_{||u}$ are plotted in figure 4(b) and will be discussed in section 3.

This definition for $q_{||u}$ (as the simulated $q_{||}$ at the outer divertor entrance of SOL ring 3) was chosen to allow a fair comparison between the Lengyel models and the simulations, for the operationally limiting flux ring 3. Of course, a user of the Lengyel models would ideally like to have a procedure to relate the power through the separatrix to $q_{||u}$. However, this relationship depends on both the radial position of the operationally limiting flux ring, as well as λ_q . Both of these quantities are themselves dependent on the radial transport, which in these simulations was prescribed via

anomalous diffusive transport coefficients. In addition, convective energy fluxes due to drifts are likely to affect $q_{||u}$ in some circumstances (e.g. [20, 21]), but are not considered here.

Predictions of detachment onset using the Lengyel models must therefore resort to some other model to relate the power crossing the separatrix to $q_{||u}$ in the operationally limiting flux ring, none of which are currently very satisfactory. One simple approach would be to calculate λ_q from the Eich scaling [22], as done in [12, 13], then assume that the operationally-limiting flux tube lies at a distance $\sim \lambda_q$ from the separatrix, as was found in section 2.2. In addition, in the absence of drift

simulations for the machine being predicted, the in/out power asymmetry must also be assumed. Unfortunately, the validity of the Eich scaling may break down on future machines, and (as has already been mentioned) the position of the operationally-limiting flux tube found here is dependent on the particular anomalous diffusivities chosen for these simulations.

2.3.2. c_{Ne} . The neon concentration c_{Ne} was taken as the total number of neon particles (all charge states including neutral neon) divided by the total number of electrons, in the outer divertor portion of the third SOL ring (highlighted in magenta in figure 1)(c). We label this quantity $\langle c_{\text{Ne}} \rangle_{\text{div}}$. In the constant $\langle c_{\text{Ne}} \rangle_{\text{sep}}$, variable P_{in} simulations (horizontal ticks in table 1), the simulated $\langle c_{\text{Ne}} \rangle_{\text{div}}$ was held approximately constant (at least at rollover, where we are most interested in the comparison to the Lengyel models; see figure 2)(b). In those cases, the simulated $\langle c_{\text{Ne}} \rangle_{\text{div}}$ was an input to the Lengyel models. Meanwhile, in the constant P_{in} , variable $\langle c_{\text{Ne}} \rangle_{\text{sep}}$ simulations (vertical ticks in table 1), the simulated $\langle c_{\text{Ne}} \rangle_{\text{div}}$ varied significantly and was compared to the output of the Lengyel models. Since in these cases $\langle c_{\text{Ne}} \rangle_{\text{div}}$ was regarded as an output of the Lengyel models rather than an input, we do not plot it in figure 2; the simulated $\langle c_{\text{Ne}} \rangle_{\text{div}}$ are plotted in figure 4(a) and will be discussed in section 3.

Again, this choice to use the average neon concentration in the outer divertor third SOL ring was made to allow a fair comparison between the Lengyel models and the simulations; the Lengyel models predict the impurity concentration in the region where impurities are acting, which is inside the divertor in these simulations (see the lower plots in figure 9). However, the more *operationally relevant* quantity will be the upstream $\langle c_{\text{Ne}} \rangle_{\text{sep}}$, since that measures the concentration of neon next to closed flux surfaces¹⁰. In the simulations, there do exist significant parallel gradients in c_{Ne} (see figure 15). However, for now, to allow a fair assessment of the Lengyel models, we use the simulated *divertor* concentration $\langle c_{\text{Ne}} \rangle_{\text{div}}$ for our comparisons. This important issue will be revisited in section 6, where we will also repeat the comparison presented in this section, but using more operationally relevant quantities for the neon concentration and electron density.

2.3.3. n_{eu} . In the comparisons that follow, n_{eu} was used as an input to the Lengyel models and was set equal to the simulated electron density at the outer divertor entrance for the third SOL ring, $n_{\text{e,div.ent.ring3}}$. As above, we chose this position for n_{eu} because it is the most relevant one for a fair comparison to the Lengyel model in the third SOL ring. The most *operationally relevant* upstream densities, however, will be values on the *first* SOL ring. Here, we consider: (i) the average n_{e} in the first SOL ring above the x-point, $\langle n_{\text{e}} \rangle_{\text{sep}}$; (ii) the maximum n_{e} anywhere above the x-point on the first SOL ring, $\max(n_{\text{e,sep}})$ (note that this maximum always occurs in one of the two cells

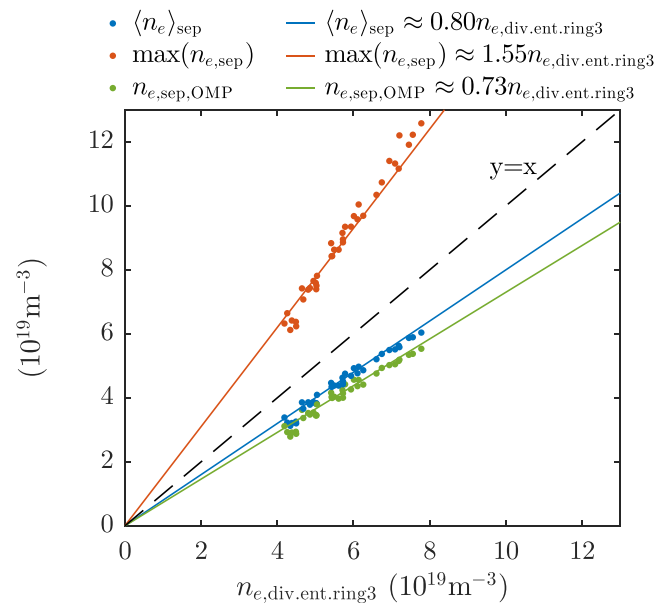


Figure 3. Linear dependence between operationally relevant upstream electron densities on the first SOL ring and $n_{\text{e,div.ent.ring3}}$. The latter was chosen as the fairest position for comparison to the Lengyel models. The entire database is shown, with equations for the lines of best fit given at the top of the figure. The $y = x$ line is also given for reference.

closest to the x-point, usually on the inboard side); (iii) n_{e} at the outer mid-plane first SOL ring, $n_{\text{e,sep,OMP}}$. These quantities are plotted in figure 3, as a function of $n_{\text{e,div.ent.ring3}}$. The important thing to note is that each of these operationally relevant upstream densities has a linear relationship with $n_{\text{e,div.ent.ring3}}$ (the equations for the lines of best fit are given at the top of the figure). Thus, *scaling* comparisons to the Lengyel models will be minimally affected by a more operationally relevant choice of n_{eu} , although *absolute* comparisons will be slightly affected.

2.3.4. Other input parameters. In addition to n_{eu} , $q_{\parallel\text{u}}$ and c_{Ne} , the remaining inputs to the Lengyel models were defined as follows:

- $\kappa_{\text{e}\parallel\text{0,FL}}$. The Lengyel model input $\kappa_{\text{e}\parallel\text{0,FL}}$ was set to the parallel-averaged, flux-limited value in the third SOL ring, $\langle \kappa_{\text{e}\parallel\text{0,FL}} \rangle_{\text{div}}$. Figure 2(c) shows $\langle \kappa_{\text{e}\parallel\text{0,FL}} \rangle_{\text{div}}$ for the entire database (blue dots), as well as the non-flux-limited values, $\langle \kappa_{\text{e}\parallel\text{0}} \rangle_{\text{div}}$ (red dots). Except for the two most impure cases, there is a variation of 30% in $\langle \kappa_{\text{e}\parallel\text{0,FL}} \rangle_{\text{div}}$. Other users of the Lengyel model might justifiably choose alternative schemes to account for the impact of kinetic effects and impurities on $\kappa_{\text{e}\parallel\text{0}}$, different to those used in these simulations¹¹. Our interest here is not in discrepancies between the code and the Lengyel model which arise because of changes in $\langle \kappa_{\text{e}\parallel\text{0,FL}} \rangle_{\text{div}}$. We therefore use the

¹⁰ Note that by an ‘operationally relevant’ quantity we do not mean to imply that the quantity will be directly controllable during operations. We just mean that the quantity plays an important role in setting the tokamak’s operational range.

¹¹ With the settings used for these simulations (no longer the defaults in the more recent SOLPS-ITER code), $\kappa_{\text{e}\parallel\text{0}} = 2597/Z_{\text{eff}}$ was used. As recognised in [23] this is a ‘simplification of the complete multispecies transport theory’. An electron heat flux limiter of $\alpha_{\text{e}} = 0.2$ was also chosen.

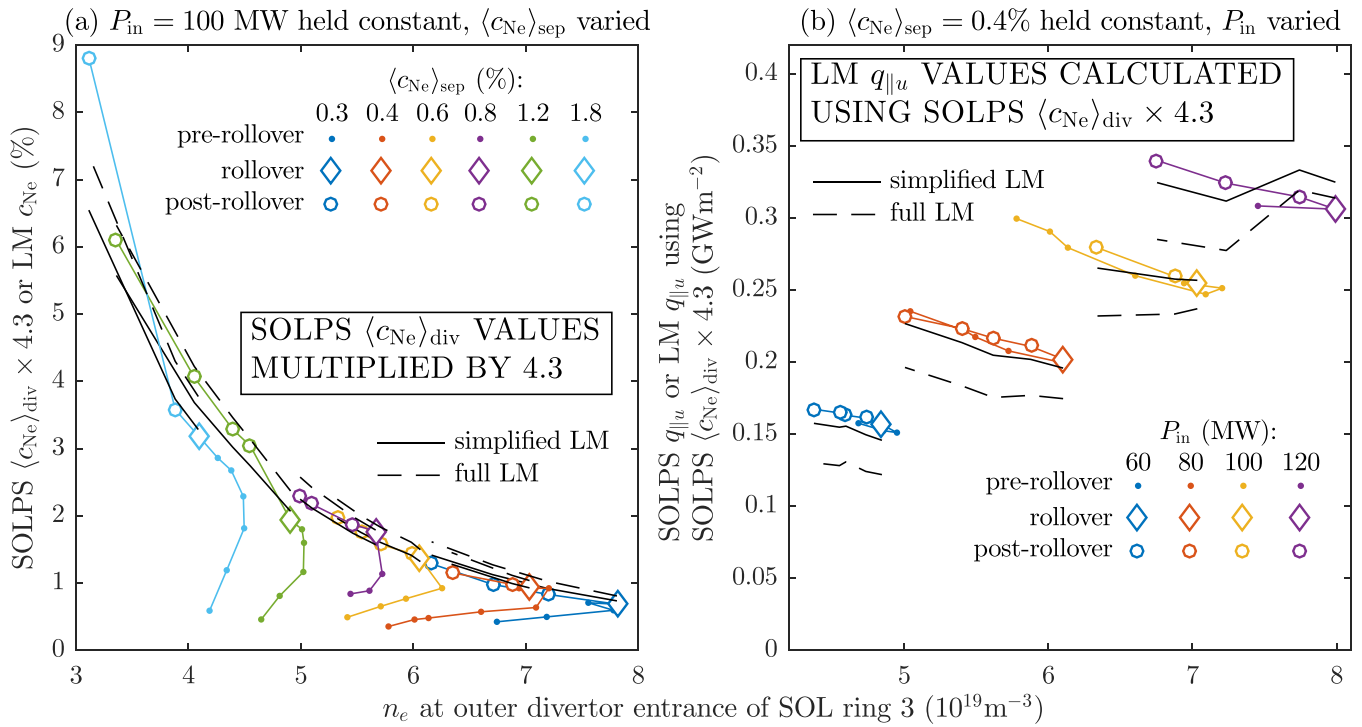


Figure 4. Comparison between SOLPS and the Lengyel model (‘LM’ in this figure) predictions, for the third SOL flux ring. (a) Comparison of the predicted and simulated neon concentrations in the outer divertor, for the six puff scans between which $\langle c_{\text{Ne}} \rangle_{\text{sep}}$ is varied and P_{in} is held constant. (b) Comparison of the predicted and simulated parallel plasma energy flux density entering the outer divertor, for the four puff scans between which P_{in} is varied and $\langle c_{\text{Ne}} \rangle_{\text{sep}}$ is held constant. All simulations leading up to, at, and after outer target flux rolover for this ring are shown (see legends).

$\langle \kappa_{e\parallel 0, \text{FL}} \rangle_{\text{div}}$ value for each simulation as input to its corresponding Lengyel model calculation.

- $L_{\text{Ne}}^{n_e \tau}$. To calculate $L_{\text{Ne}}^{n_e \tau}$, we took the same ionisation and recombination rates for neon that were used in these SOLPS-4.3 simulations (again from the STRAHL database). Those rates, along with a fixed $n_e \tau$ value, were used as inputs to an ionisation balance calculation (implemented with code from the ADAS library and based on the original work by [17]). Based on the analysis that will be presented in section 5, we chose $n_e \tau = 0.5 \times 10^{20} \text{ m}^{-3} \text{ ms}$. The resulting fractional abundances $F_{\text{Ne}_z}^{n_e \tau}$ were then used to calculate $L_{\text{Ne}}^{n_e \tau} = \sum_{z=0}^{10} F_{\text{Ne}_z}^{n_e \tau} \eta_{\text{Ne}_z}^{\text{STRAHL}}$. In this way, the $L_{\text{Ne}}^{n_e \tau}$ functions used in the Lengyel model calculations were consistent with the neon rates used in the SOLPS-4.3 simulations. Thus, any discrepancies between $L_{\text{Ne}}^{\text{SOLPS}}$ and $L_{\text{Ne}}^{n_e \tau}$ can be attributed to a more physical description of the neon transport in SOLPS-4.3, rather than differences in the rates (see section 5 for more details).
- L_{\parallel} . We took $L_{\parallel} = 20.0 \text{ m}$ from the simulation grid as the parallel distance from outer divertor entrance to target in the third SOL ring.
- T_{et} and γ . For the full Lengyel model, $T_{\text{et}} = 1.8 \text{ eV}$ was used as an input, based on the outer target rolover temperature for SOL flux ring 3 (this was the mean rolover temperature in the last numerical cell before the guard cell; the standard deviation was 0.4 eV). Note that, at most, the calculated full Lengyel model values were altered by only 5% when the actual T_{et} in the SOLPS simulation was

used instead of 1.8 eV. For the sheath heat transmission coefficient, these simulations assumed a value of 5.1 for the electrons¹² and 3.5 for the ions. On this basis we set $\gamma = 8.6$ as input to the full Lengyel model. For the simplified Lengyel model, no input was required for either T_{et} or γ because $q_{\parallel t} = T_{\text{et}} = 0$ is assumed.

3. The comparison

Let us now compare the Lengyel model predictions of the $(c_{\text{Ne}}, q_{\parallel u}, n_{\text{eu}})$ detachment points to the SOLPS-4.3 simulations. Figure 4(a) compares predictions of c_{Ne} as a function of n_{eu} for simulations in which $q_{\parallel u}$ was held approximately constant by fixing P_{in} ; third column in table 1. Figure 4(b) compares predictions of $q_{\parallel u}$ as a function of n_{eu} for simulations in which $\langle c_{\text{Ne}} \rangle_{\text{div}}$ was held approximately constant (at least for the outer target rolover points) by fixing $\langle c_{\text{Ne}} \rangle_{\text{sep}}$; second row in table 1.

Different colours in figure 4 represent different puff scans, as labelled. Data is plotted throughout the entirety of each puff scan, rather than just at the rolover points where we expect the Lengyel model predictions to best match the simulations. Simulations before rolover in the outer target D⁺

¹² In actual fact, the code takes as input an additional contribution to the electron energy transmission coefficient, specified here as 2.0, in addition to the sheath potential. The sheath potential does depend on T_i/T_e , but in practice this dependence is sufficiently weak that, to a good approximation, the electron sheath energy transmission coefficient was 5.1 for all simulations.

flux of the third SOL ring are shown as dots, simulations at rollover are shown as diamonds and simulations after rollover are shown as open circles. For comparison, the simplified and full Lengyel model predictions are given by the solid and dashed black lines, respectively. We only calculate the Lengyel model predictions for simulations at or after rollover. See appendix B for a discussion of the pre-rollover phase, in which we introduce the dissipated power fraction as an additional parameter to the simplified Lengyel model. Note that in figure 4(a) we have multiplied the SOLPS-simulated $\langle c_{\text{Ne}} \rangle_{\text{div}}$ values by a factor 4.3, while for consistency in figure 4(b) we have used the simulated $\langle c_{\text{Ne}} \rangle_{\text{div}} \times 4.3$ as input to the Lengyel model calculations. The reasons why this factor 4.3 is necessary to achieve good agreement between the simulations and the Lengyel model predictions will be discussed in detail in section 4.

Three observations can be made regarding figure 4:

- For simulations at rollover, the Lengyel models do a remarkably good job of predicting the simulated variation of both $\langle c_{\text{Ne}} \rangle_{\text{div}}$ and q_{\parallel} with $n_{e,\text{div.ent.ring3}}$, once the SOLPS-4.3 $\langle c_{\text{Ne}} \rangle_{\text{div}}$ is multiplied by a factor 4.3.
- Even beyond rollover, the Lengyel models continue to predict the required $\langle c_{\text{Ne}} \rangle_{\text{div}}$ vs $n_{e,\text{div.ent.ring3}}$ with the same overprediction factor. *The decrease in upstream density after detachment is consistent with the increase in $\langle c_{\text{Ne}} \rangle_{\text{div}}$, such that the Lengyel model scaling is still met.* It remains to be seen at what degree of detachment the Lengyel model scaling breaks down; more strongly-puffed cases are in progress to assess this.
- The simplified and full Lengyel models predict very similar values of c_{Ne} and q_{\parallel} . In fact, the c_{Ne} prediction is consistently a factor 1.14 ± 0.01 larger in the full model, while the q_{\parallel} prediction is a factor 1.14 ± 0.05 lower. This agrees with the small difference between the full and simplified Lengyel models previously found in [12], and is a result of a slightly higher $T_{e\text{u}}$ prediction from the two-point model compared to the full Lengyel model. Given this small discrepancy, and the fact that the simplified Lengyel model is easier to analyse, we focus our analysis below on the comparison to the simplified Lengyel model.

4. Analysis of the comparison

In the following analysis, unless otherwise stated, we focus on the comparison between SOLPS-4.3 and the simplified Lengyel model at outer target ion flux rollover in the third SOL ring (diamonds in figure 4).

4.1. Overview of the extra physics in SOLPS-4.3 leading to a 4.3 times lower required impurity concentration for rollover

Our goal in this section is to broadly evaluate which additional physics in SOLPS-4.3 leads to the approximately constant factor ~ 4.3 reduction in the simulated divertor neon concentration required for rollover, compared to that predicted by the simplified Lengyel model.

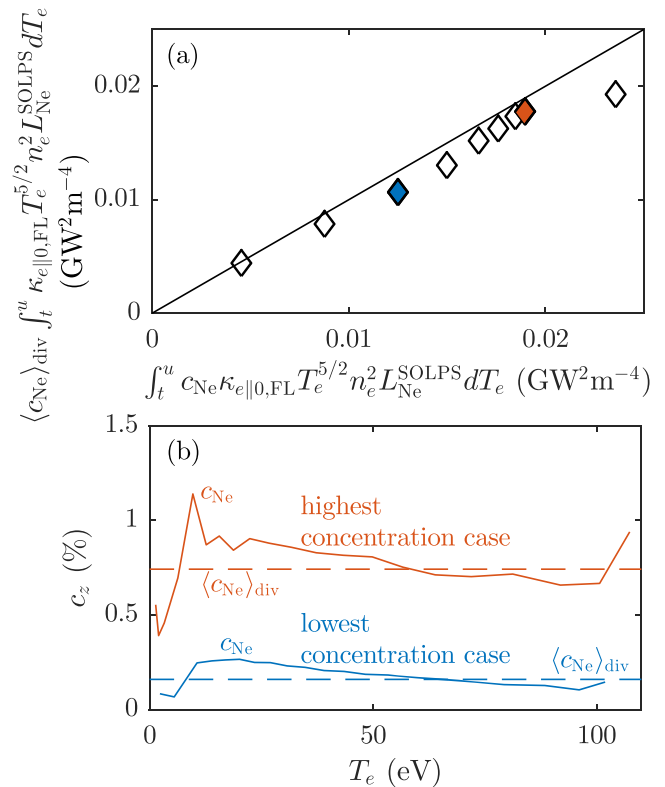


Figure 5. Justification for setting $c_{\text{Ne}} = \langle c_{\text{Ne}} \rangle_{\text{div}}$ in our analysis. (a) The integral in (10) (x-axis) is compared to its value when c_{Ne} is set equal to $\langle c_{\text{Ne}} \rangle_{\text{div}}$ (y-axis), for the third SOL ring at flux rollover for all nine D_2 puff scans in the database. (b) The $c_{\text{Ne}}(T_e)$ profiles in the highest and lowest seeded simulations (as highlighted in (a)), compared to the average $\langle c_{\text{Ne}} \rangle_{\text{div}}$ value. Profiles are shown up to the outer divertor entrance.

It is useful for our analysis (as well as for the Lengyel models) to assume that c_{Ne} in the outer divertor is constant along the flux ring of interest, i.e. $c_{\text{Ne}} = \langle c_{\text{Ne}} \rangle_{\text{div}}$.¹³ The justification for this is shown in figure 5(a), where we demonstrate that bringing c_{Ne} outside of the integral in (10) and setting it to $\langle c_{\text{Ne}} \rangle_{\text{div}}$ (y-axis) has only a small effect on the integral itself (x-axis). We therefore draw the important conclusion that the Lengyel model assumption of poloidally constant c_{Ne} within the outer divertor is not responsible for the difference between Lengyel model concentrations and the simulated $\langle c_{\text{Ne}} \rangle_{\text{div}}$. For completeness, in figure 5(b) we show the actual $c_{\text{Ne}}(T_e)$ profiles for the rollover points in the lowest and highest neon concentration scans (as highlighted in the appropriate colour in figure 5(a)). These profiles are plotted alongside the $\langle c_{\text{Ne}} \rangle_{\text{div}}$ value for that simulation, in the outer divertor third SOL ring up to the outer divertor entrance. Note that, as discussed in section 6, the neon concentration does increase in the main SOL. We see from this analysis, however, that it is sufficiently constant *within* the outer divertor third SOL ring to assume $c_{\text{Ne}} = \langle c_{\text{Ne}} \rangle_{\text{div}}$.

¹³ recall from section 2.3.2 that $\langle c_{\text{Ne}} \rangle_{\text{div}}$ is defined as the total number of neon particles (all charge states including neutral neon) divided by the total number of electrons, in the outer divertor portion of the third SOL ring.

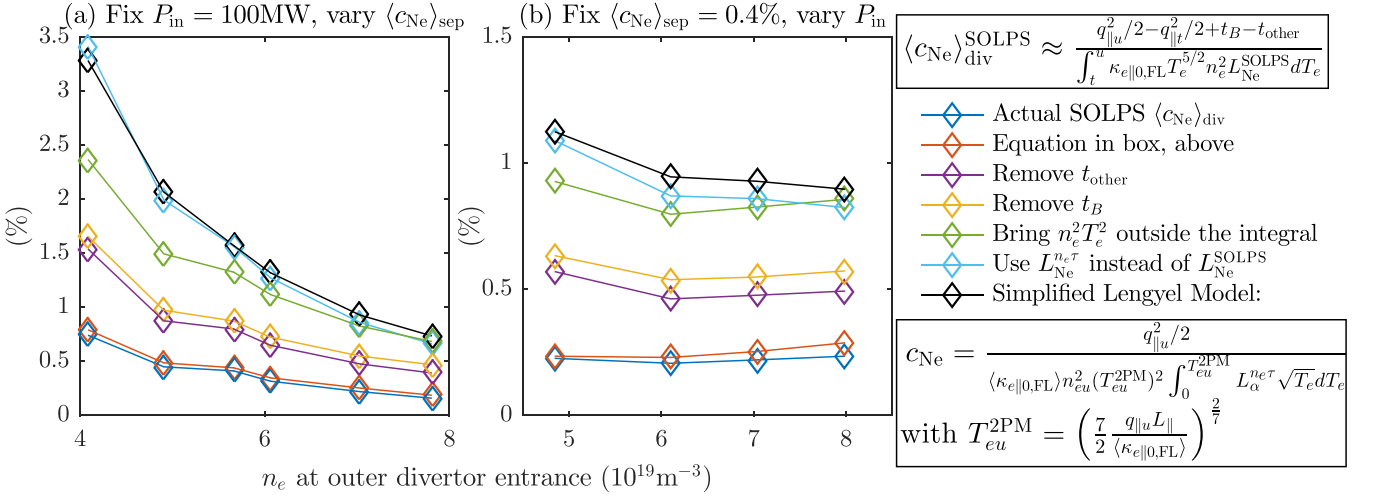


Figure 6. The importance of the assumptions that are made in the simplified Lengyel model but are not made in SOLPS-4.3, with regard to the divertor neon concentrations that they predict. The calculated neon concentrations are shown as a function of $n_{e,div.ent.ring3}$, for (a) the fixed P_{in} simulations and (b) the fixed $\langle c_{Ne} \rangle_{sep}$ simulations. The simplified Lengyel model assumptions are gradually imposed on the SOLPS-4.3 equation (19) (top right box), until it becomes the simplified Lengyel model equation (17) (bottom right box). Only simulations at ion target flux rollover are considered.

Setting $c_{Ne} = \langle c_{Ne} \rangle_{div}$, equation (10) can now be rearranged to give

$$\langle c_{Ne} \rangle_{div} \approx \frac{q_{||u}^2/2 - q_{||t}^2/2 + t_B - t_{other}}{\int_t^u \kappa_{e||0,FL} T_e^{5/2} n_e^2 L_{Ne}^{SOLPS} dT_e}, \quad (19)$$

where the limits of the integral are taken directly from the code, at the target and at the outer divertor entrance. By progressively moving from the SOLPS-4.3 equation (19) to the simplified Lengyel model equation (17), we can better understand which assumptions in the Lengyel model cause it to predict a factor ~ 4.3 higher divertor neon concentration. Figure 6 shows just such a progression for (a) the fixed P_{in} , variable $\langle c_{Ne} \rangle_{sep}$ scans at rollover and (b) the fixed $\langle c_{Ne} \rangle_{sep}$, variable P_{in} scans at rollover. The blue diamonds show the actual $\langle c_{Ne} \rangle_{div}$ values calculated from the simulations, which compare well to equation (19), plotted as red diamonds (within a factor ~ 1.1).

Next, we remove the t_{other} term from equation (19) and plot the resulting concentration as purple diamonds. Recall that this term accounts for other heat flux mechanisms besides electron conduction, as well as other heat loss mechanisms besides neon cooling. Removing it significantly increases the calculated concentration (i.e. these mechanisms act to reduce the required concentration in the simulations), by a factor ~ 2 . This term will be investigated in more detail in section 4.2.

Next, we remove the t_B term as well and recalculate the concentrations (yellow diamonds). Recall that this term, given by equation (11), accounts for variation in the magnetic field strength along the divertor leg. As expected for the ITER divertor, with only a $\sim 10\%$ increase in the outer target strike point major radius compared to the x-point major radius, removing the t_B term has little effect (a factor ~ 1.1 increase in the calculated concentration). Note that a proper consideration of this term would be necessary for

‘Super-X’ divertors with strong variation in B along the divertor leg [24].

Next, plotted as green diamonds, we bring the $n_e^2 T_e^2$ term outside the integral in the denominator of (19) and assume electron pressure conservation. So now the denominator is $n_{eu}^2 T_{eu}^2 \int_t^u \kappa_{e||0,FL} T_e^{1/2} L_{Ne}^{SOLPS} dT_e$. The upstream electron temperature (outer divertor entrance) is still taken from the code output at this stage. This assumption also moves the calculated concentration up significantly towards the simplified Lengyel model result (by a factor ~ 1.5), suggesting that the electron pressure increases in the simulation from its upstream value to the radiating region. This effect will be investigated further in section 4.3.

Next, we replace the code-calculated neon cooling function L_{Ne}^{SOLPS} with $L_{Ne}^{n_e \tau}$ at $n_e \tau = 0.5 \times 10^{20} \text{ m}^{-3} \text{ ms}$. The resulting concentrations are plotted as cyan diamonds. We see that this has only a small effect on the calculated concentrations for the fixed $\langle c_{Ne} \rangle = 0.4\%$, variable P_{in} scans, but a more significant effect on the *scaling* of the calculated concentrations for the fixed $P_{in} = 100 \text{ MW}$, variable $\langle c_{Ne} \rangle$ scans. In particular, the lower density concentration calculations are pushed higher while the high density concentration calculations remain approximately where they were. This will be investigated further in section 5. Note that the overall scaling comparison to the Lengyel model is still good, because the other assumptions (poloidally constant neon concentration and electron pressure, $t_{other} = t_B = 0$) combine to cancel out the change in scaling brought about by assuming $L_{Ne}^{SOLPS} = L_{Ne}^{n_e \tau}$.

In the final step (black diamonds), we combine a number of simplifications (none of which have a significant impact on the calculated concentration), as follows. We remove the $q_{||t}^2/2$ term, but this is small because at rollover most of the incoming $q_{||u}$ is either radiated, transported radially, consumed by ionisation, or transferred to neutrals. We take $\kappa_{e||0,FL}$ outside

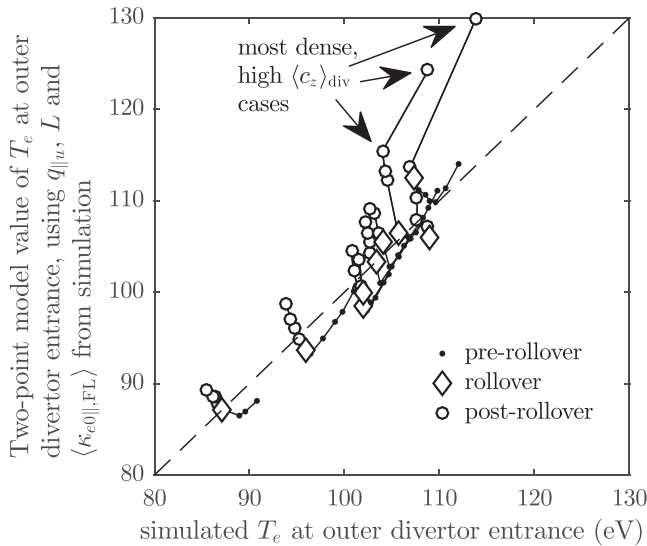


Figure 7. Accuracy of the two point model formula for T_{eu} (y-axis) compared to the simulated value at the outer divertor entrance, 3rd SOL ring (x-axis). All 72 simulations are shown before, at and after rollover, as labelled.

the integral and replace it with its parallel average. But the effect of this is small because $\kappa_{e||0}$ is a function only of Z_{eff} in the code, and Z_{eff} does not vary significantly in the parallel direction. We also switch the limits of the integral from the code-calculated limits to the simplified Lengyel model limits (recall that the simplified Lengyel model limits go from zero to the two-point model formula for the divertor entrance temperature T_{eu}^{2PM}). But, because T_{eu}^{2PM} is a good approximation to T_{eu} in the simulations (figure 7), and because neon cooling is negligible between zero and the simulated T_{et} , the effect of this is small¹⁴.

After this final step, we are back to the simplified Lengyel model, repeated for convenience in the bottom right box of figure 6. We now consider in more detail the important simplifications highlighted above.

4.2. Effect of other heat flux and heat loss mechanisms

Consider again the term t_{other} , which acts via alternative heat flux and loss mechanisms to reduce the required $\langle c_{Ne} \rangle_{div}$ in the simulations (larger t_{other} leads to lower $\langle c_{Ne} \rangle_{div}$). Using equation (1) we have

$$\begin{aligned} t_{other} &= \int_t^u B q_{||other} d\left(\frac{q_{||}}{B}\right) + \int_t^u \kappa_{e||0} T_e^{5/2} S_{Qother} dT_e \\ &= \int_t^u q_{||other} S_{QNe} ds + \int_t^u q_{||other} S_{Qother} ds \\ &\quad + \int_t^u \kappa_{e||0} T_e^{5/2} S_{Qother} dT_e, \end{aligned} \quad (20)$$

where we recall that

¹⁴Note that the only significant deviation from the two-point model occurs for the most dense, highest impurity concentration cases, in which there is significant radiation upstream.

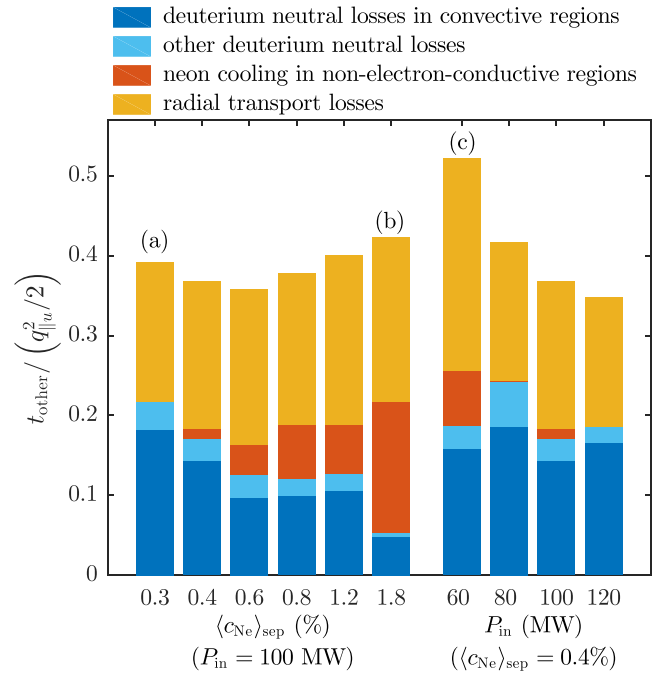


Figure 8. Decomposition of the t_{other} term in equation (19), normalised to $q_{||u}^2/2$. The heat balance along the outer divertor third ring for simulations (a)–(c) are shown in figure 9.

$$q_{||other} = q_{||e,conv} + q_{||i,cond} + q_{||i,conv},$$

$$S_{QNe} = n_e^2 c_{Ne} L_{Ne}^{SOLPS},$$

$$S_{Qother} = S_{Qneut} + S_{QRT}.$$

Before analysing the composition of t_{other} in the simulations, it is worth noting that $q_{||other}$ and S_{Qother} have the potential to act not only through t_{other} but also indirectly via the limits of the integral in the denominator of (19), in particular by changing T_{eu} . For the case where $q_{||other}$ or S_{Qother} are significant upstream, this effect can outweigh the t_{other} term. For the simulations considered here, however, the upstream $q_{||other}$ and S_{Qother} are sufficiently small so as not to push T_{eu} too far from the two-point model value (recall figure 7). In these cases, therefore, the effects of alternative heat flux and loss mechanisms are mostly captured in t_{other} . Note that drift effects may change this picture significantly, but are not considered here.

Figure 8 shows a bar chart of $t_{other} / (q_{||u}^2/2)$ in the simulations at rollover for the third SOL ring in the outer divertor. Normalising to $q_{||u}^2/2$ allows us to see the importance of t_{other} relative to the numerator in the simplified Lengyel model for c_{Ne} . We see that the total $t_{other} / (q_{||u}^2/2)$ is around ~ 0.4 – 0.5 , consistent with the factor ~ 2 increase in calculated concentration when t_{other} was removed in figure 6 (red to purple diamonds).

Figure 8 also gives the components of t_{other} due to neutral losses (dark and light blue), neon cooling in non-electron-conductive regions (red), and radial transport losses (yellow). As an aid to explain these components, figure 9 shows the heat balance along the third SOL ring, for the three simulations labelled ‘(a)’, ‘(b)’ and ‘(c)’ in figure 8. Among the

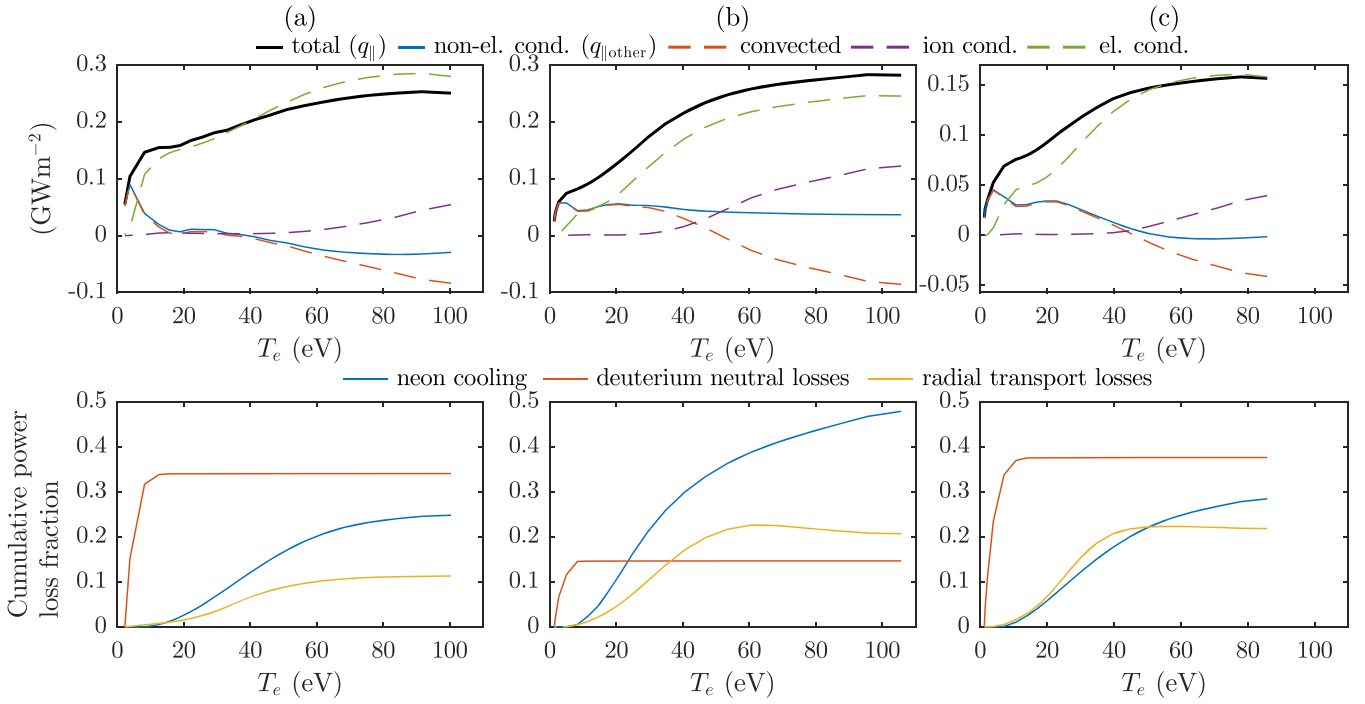


Figure 9. Heat balance along the third SOL ring at ion flux rollover, for the three simulations labelled ‘(a)’, ‘(b)’ and ‘(c)’ in figure 8. Upper plots show the decomposition of the heat flux, while lower plots show the decomposition of the heat losses. These heat losses are plotted as cumulative fractions of the total heat flux entering the outer divertor (increasing away from the target). The sum of the blue, red and yellow lines at their rightmost positions gives the total power loss fraction for the entire outer divertor flux third SOL ring.

simulations at target flux rollover, these three were selected for a more detailed analysis because they exhibit the largest variation in their heat balance components. Figure 9 will be discussed in conjunction with figure 8.

The deuterium neutral loss contribution plotted in figure 8 is given by

$$t_{\text{other, neut}} = \int_t^u q_{\parallel\text{conv}} S_{Q_{\text{neut}}} ds + \int_t^u q_{\parallel\text{icond}} S_{Q_{\text{neut}}} ds + \int_t^u \kappa_{e||0} T_e^{5/2} S_{Q_{\text{neut}}} dT_e, \quad (21)$$

where $q_{\parallel\text{conv}} = q_{\parallel\text{e,conv}} + q_{\parallel\text{i,conv}}$ is the total (electron plus ion) parallel convective energy flux density. The first term in (21) is plotted in dark blue and the sum of the second and third terms is plotted in light blue in figure 8. We see that the first term is dominant, i.e. neutrals reduce the required $\langle c_{\text{Ne}} \rangle_{\text{div}}$ by reducing the total heat flux in convective regions. As shown in figure 9, the neutral losses are almost entirely localised to near-target regions below 10 eV, while significant target-directed convective flows can contribute to $q_{\parallel\text{other}}$ further upstream as well, up to ~ 40 eV for the highest seeded case (b) and for the lowest power case (c). These convective flows upstream of the neutral interaction region are linked to strong anomalous transport of parallel momentum from the second flux tube¹⁵.

It is worth noting that, even for case (a) where deuterium neutrals remove 1.4 times more power from this flux tube than

neon, the neutral loss only contributes $\sim 0.1q_{\parallel\text{u}}^2$ to t_{other} , corresponding to just a ~ 1.25 times increase in the calculated neon concentration when neutral losses are excluded. Note also that in figure 8 the magnitude of the neutral loss term is reduced at higher impurity concentrations, because more of the work to reduce $q_{\parallel\text{t}}$ is being done by impurity radiation. However, in these simulations, the reduced neutral loss term is compensated by neon cooling in non-electron-conductive regions upstream. This term, shown in red in figure 8, is given by

$$t_{\text{other, Ne}} = \int_t^u q_{\parallel\text{conv}} S_{Q_{\text{Ne}}} ds + \int_t^u q_{\parallel\text{icond}} S_{Q_{\text{Ne}}} ds. \quad (22)$$

Both components of $t_{\text{other, Ne}}$ become significant at high $\langle c_{\text{Ne}} \rangle_{\text{sep}}$ [in particular for the highest seeded case (b)] because there are regions of convection (as noted above) and also strong ion conduction (due to the reduced density and therefore reduced electron-ion equipartition) in the neon-radiating regions. Both of these features can be seen in figure 9(b).

Consider now the radial transport loss contribution, shown in yellow in figure 8 and given by

$$t_{\text{other, RT}} = \int_t^u q_{\parallel\text{conv}} S_{Q_{\text{RT}}} ds + \int_t^u \kappa_{e||0} T_e^{5/2} S_{Q_{\text{RT}}} dT_e + \int_t^u q_{\parallel\text{icond}} S_{Q_{\text{RT}}} ds. \quad (23)$$

The third term in (23) is always negligible for these simulations and in this flux tube, because radial transport occurs at lower temperatures than ion conduction. Typically, the second term in (23) is dominant (although for the cases labelled ‘(b)’ and

¹⁵ Note that the negative $q_{\parallel\text{conv}}$ values seen in figure 9 are a result of main ion flow reversal, apparently due to ‘overionisation’ in the near-SOL flux tubes. See chapter 15 of [18] and references therein.

‘(c)’ in figure 8, there is also a significant contribution from the first term due to radial transport in the extended convective region).

Overall, the effect of radial transport is fairly constant across the puffing scans at rollover for this flux tube. It is not possible, however, to offer any guidance regarding radial transport due to its prescribed and diffusive nature in the simulations; predictive (turbulent) transport simulations will be required for that. We can only state that in the simulations presented here, with the anomalous diffusivities chosen here, the effect of radial transport on the simulated $\langle c_{\text{Ne}} \rangle_{\text{div}}$ at rollover is of similar order to the effect of deuterium neutrals at low seeding levels, and more important than deuterium neutrals at high seeding levels.

It is worth discussing here the importance of deuterium neutral effects on the values of $(c_{\text{Ne}}, q_{\parallel u}, n_{\text{eu}})$ at which the target ion flux rolls over (the ‘rollover point’). We know on current machines that increased deuterium neutral trapping in the divertor can aid detachment onset; see as examples [25] and references therein, as well as the more recent analysis on TCV [26] and DIII-D [27–29]. However, the Lengyel models outlined in section 1 have no way of capturing this physics, implying that extensions are necessary to capture neutral effects on current machines. Fortunately, from the point of view of applying the Lengyel models to ITER, the simulations analysed here suggest that the neutral loss fraction is sufficiently small on ITER that neutrals have a relatively weak effect on the required $(c_{\text{Ne}}, q_{\parallel u}, n_{\text{eu}})$ for rollover, i.e. extensions to capture neutral physics are not critical when applying Lengyel models to ITER.

It may seem counterintuitive that deuterium neutrals result in only a small change to the upstream $(c_{\text{Ne}}, q_{\parallel u}, n_{\text{eu}})$ rollover point while still exhausting a significant fraction of the input power to a flux ring (recall that in some simulations the neutral loss fraction even exceeds the neon cooling fraction, figure 9). To understand this further, consider the case where neutrals remove the entire second half of the input $q_{\parallel u}$ in an entirely convective region near the target, where the impurity cooling is negligible. In that case, $\int_0^u q_{\parallel \text{conv}} S_{Q_{\text{neut}}} ds = \int_0^{q_{\parallel u}/2} q_{\parallel} dq_{\parallel} = q_{\parallel u}^2/8$, resulting in only a 25% reduction in the required c_{Ne} , or equivalently a 13% reduction in the required n_{eu} . We conclude from this analysis that, for the current machines which are strongly influenced by changes in neutral trapping, the neutral loss fraction must be significantly higher than in the ITER simulations analysed here. Indeed, one can see a general trend in figure 8 whereby the impact of neutrals increases as neon concentration decreases and the neutral loss fraction increases. This suggests that for even lower neon concentrations than explored here, neutral losses would start to play an important role in setting the upstream $(c_{\text{Ne}}, q_{\parallel u}, n_{\text{eu}})$ rollover point. However, such low concentrations are likely to require inaccessible upstream densities due to the Greenwald density limit.

None of this is to suggest that deuterium neutral losses are not generally important. If the neutral loss fraction can be raised significantly above ITER’s on some other reactor, for example by use of a small-angled slot divertor [30–33], the rollover point will likely be affected by neutral losses. In such

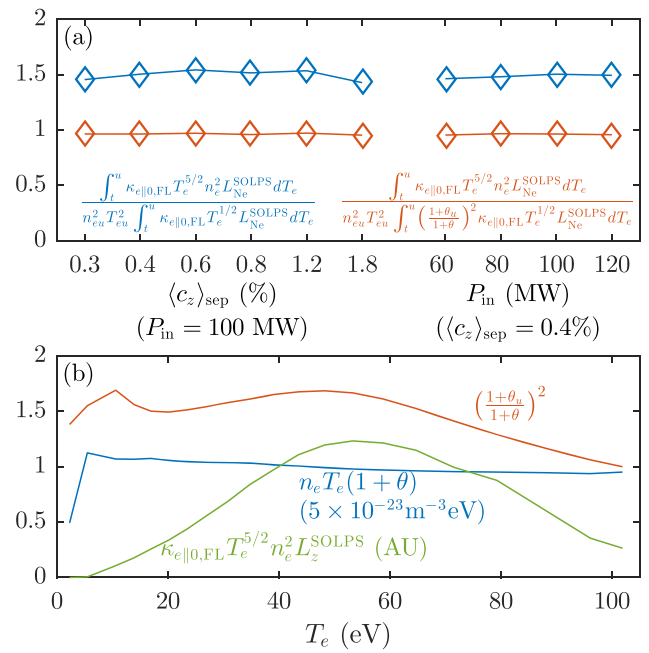


Figure 10. The importance of including ion temperature when assuming static pressure conservation along the outer divertor leg. (a) Blue diamonds: the denominator of (19) divided by the same quantity with $n_e^2 T_e^2$ brought outside the integral and set to $n_{\text{eu}}^2 T_{\text{eu}}^2$. Red diamonds: the denominator of (19) divided by the same quantity with $n_e^2 T_e^2$ brought outside the integral and set to $n_{\text{eu}}^2 T_{\text{eu}}^2$, and with the function $(1+\theta_u)^2/(1+\theta)^2$ left inside the integral. Here, $\theta = T_i/T_e$. (b) Blue line: electron plus ion static pressure along the outer divertor third SOL ring at rollover. Red line: the function $(1+\theta_u)^2/(1+\theta)^2$. Green line: the integrand in the denominator of (19). All plots in (b) are for the $\langle c_{\text{Ne}} \rangle_{\text{sep}} = 0.3\%$, $P_{\text{in}} = 100$ MW case at rollover.

cases, extensions to the Lengyel models to include deuterium neutral losses will be necessary. We also note the critical role of deuterium neutrals in removing any residual heat flux not removed by impurity radiation, which can still be sufficient to exceed tolerable target loads.

4.3. Effect of poloidally-varying electron pressure

We saw in figure 6 that making the Lengyel model assumption of constant electron pressure along the outer divertor ring, so that $n_e^2 T_e^2$ can be brought outside the integral in the denominator of (19), results in a ~ 1.5 times increase in the calculated neon concentration. In fact, this increase is quite constant across all of the simulations. This is shown in figure 10(a) (blue diamonds), where we plot the denominator of (19) divided by the same quantity with $n_e^2 T_e^2$ brought outside the integral and set to $n_{\text{eu}}^2 T_{\text{eu}}^2$.

It should be noted that, although the electron static pressure $n_e T_e$ is not well conserved along the leg, the total static pressure $(1+\theta)n_e T_e$ (where $\theta = T_i/T_e$) is well conserved at target ion flux rollover, right up to the near target region (at which point it drops to approximately half its upstream value, as expected for total pressure conservation). This is shown in figure 10(b) (blue line) for the $\langle c_{\text{Ne}} \rangle_{\text{sep}} = 0.3\%$, $P_{\text{in}} = 100$ MW case. All other simulations show a similar

degree of flatness in the total static pressure at rollover; significant momentum loss fractions are not observed until after target ion flux rollover.

Thus, when bringing $n_e^2 T_e^2$ outside of the integral and replacing it with $n_{eu}^2 T_{eu}^2$, a function $(1 + \theta_u)^2 / (1 + \theta)^2$ should be left inside. This function is shown in figure 10(b) (red line) for the same $\langle c_{Ne} \rangle_{sep} = 0.3\%$, $P_{in} = 100$ MW case. Note that this function is not poloidally constant, because θ is not poloidally constant. In particular, its value at the divertor entrance ($=1$) is ~ 1.5 times lower than its value in the region where the integrand in the denominator of (19) (shown in green in figure 10(b)) is maximum. This corresponds to a value of $\theta = 0.9$ at the peak of the integrand, compared to $\theta_u = 1.4$ at the divertor entrance, i.e. the electrons and ions become more equilibrated towards the radiating region than they were upstream, where $T_i > T_e$.

From figure 10(a) we see that the effect of poloidally varying θ is approximately constant across the simulations at rollover in this database. On this basis, we can recommend an additional factor 1.5 in front of the integral in the denominator of (17). However, it is likely that for tokamaks sufficiently far from ITER in collisionality, this factor will be significantly different.

5. Fixed $n_e \tau$ approximations to the SOLPS electron cooling function

5.1. Basis for choosing $n_e \tau = 0.5 \times 10^{20} \text{ m}^{-3} \text{ ms}$

As stated in the introduction, one of the key assumptions in the Lengyel model is that the effect of impurity transport on the electron cooling function can be accounted for by assuming a fixed $n_e \tau$ approximation [17], so that $L_{Ne}^{SOLPS} \approx L_{Ne}^{n_e \tau} = \sum_{z=0}^{10} F_{Ne_z}^{n_e \tau} \eta_{Ne_z}^{STRAHL}$. In fact, in terms of agreement with the Lengyel model, it is primarily the extent to which $\int_t^u L_{Ne}^{SOLPS} \sqrt{T_e} dT_e \approx \int_t^u L_{Ne}^{n_e \tau} \sqrt{T_e} dT_e$ that matters.

Figure 11(a) shows, as coloured lines, $L_{Ne}^{SOLPS} \sqrt{T_e}$ for the simulations in which $P_{in} = 100$ MW was fixed and $\langle c_{Ne} \rangle_{sep}$ was varied, as labelled. As usual, values are shown for the outer divertor third SOL ring at target ion flux rollover. For comparison, we show $L_{Ne}^{n_e \tau} \sqrt{T_e}$ in black for $n_e \tau = \{0.1, 0.5, 1\} \times 10^{20} \text{ m}^{-3} \text{ ms}$. The zero transport approximation to L_{Ne} is also shown. Figure 11(b) shows the same thing for the simulations in which $\langle c_{Ne} \rangle_{sep} = 0.4\%$ was fixed and P_{in} was varied. Figure 11(c) compares the integrals of the curves in (a) and (b). It is on the basis of this plot that we chose $n_e \tau = 0.5 \times 10^{20} \text{ m}^{-3} \text{ ms}$ as input to the Lengyel model for the comparison presented in figure 4.

5.2. Observation of broadening of the electron cooling function at high $\langle c_{Ne} \rangle_{sep}$

An interesting trend is observed in figure 11(a), where L_{Ne}^{SOLPS} broadens to higher T_e with increasing $\langle c_{Ne} \rangle_{sep}$. As a result, $\int_t^u L_{Ne}^{SOLPS} \sqrt{T_e} dT_e$ increases by a factor 1.5 over the explored range of $\langle c_{Ne} \rangle_{sep}$ (left side of figure 11(c)). Compare this to $\int_t^u L_{Ne}^{n_e \tau} \sqrt{T_e} dT_e$, which remains approximately constant for each $n_e \tau$ (the small variations in $\int_t^u L_{Ne}^{n_e \tau} \sqrt{T_e} dT_e$ occur because

the temperature limits vary slightly). This is consistent with the change in scaling from the green to cyan diamonds in figure 6(a). We now consider the physical origin of this broadening of the cooling function.

5.3. Physical origin of the broadening

Figure 12 shows how $L_{Ne}^{SOLPS} = \sum_{z=0}^{10} F_{Ne_z}^{SOLPS} \eta_{Ne_z}^{STRAHL}$ is composed for the fixed P_{in} , variable $\langle c_{Ne} \rangle_{sep}$ simulations shown in figure 11(a). Figure 12(a) shows the electron cooling coefficients $\eta_{Ne_z}^{STRAHL}$ for the main cooling charge states in the third SOL ring of the outer divertor (Ne^{3+} to Ne^{7+}). These are code inputs and, for the STRAHL rates used here, are independent of density. Figures 12(b)–(f) show the fractional abundances $F_{Ne_z}^{SOLPS}$ for those same charge states, for the simulations shown in figure 11(a), and also for the fixed residence time calculations, as labelled.

Note that all of the cooling charge states have similar electron cooling coefficients, with the exception of Ne^{7+} , which radiates less efficiently since it has only one electron in its outer shell. In this region of interest then,

$$L_{Ne}^{SOLPS} \approx \langle \eta_{Ne}^{STRAHL} \rangle_{3-6} - (\langle \eta_{Ne}^{STRAHL} \rangle_{3-6} - \eta_{Ne^{7+}}^{STRAHL}) \times F_{Ne^{7+}}^{SOLPS}, \quad (24)$$

where $\langle \eta_{Ne}^{STRAHL} \rangle_{3-6}$ is the electron cooling coefficient averaged over charge states Ne^{3+} to Ne^{6+} , and the second term is positive. Thus, reducing the fractional abundance of Ne^{7+} by pushing it upstream from the outer divertor acts to maximise $\int_t^u L_{Ne}^{SOLPS} \sqrt{T_e} dT_e$. As can be seen in figures 12(b)–(f), this is exactly what happens to higher charge states with increasing $\langle c_{Ne} \rangle_{sep}$.

To understand why higher charge states are pushed further upstream with increasing $\langle c_{Ne} \rangle_{sep}$, in figures 13(a) and (c) we plot (as solid lines) the parallel velocity for Ne^{7+} ions, $u_{\parallel Ne^{7+}}$ (positive away from the target). Velocities are plotted as a function of s in the third SOL ring of the outer divertor, for the $\langle c_{Ne} \rangle_{sep}$ scan and for the P_{in} scan. Clearly, at higher $\langle c_{Ne} \rangle_{sep}$, Ne^{7+} ions have an increased parallel velocity away from the target. This is consistent with the broadening of the electron cooling functions shown in figure 11(a). By contrast, within the P_{in} scan at constant $\langle c_{Ne} \rangle_{sep}$, there is relatively little variation in the $u_{\parallel Ne^{7+}}$ profiles. This is also consistent with the lack of broadening in figure 11(b). Both of these observations can be explained by using the same analysis as [34] for ASDEX-upgrade simulations, as follows.

We assume that the ion temperature gradient force pushing impurity ions away from the target is balanced by the friction force between main ions and impurities (acting in the opposite direction). For a general impurity charge state α_z this gives

$$u_{\parallel \alpha_z} \approx u_{\parallel D^+} + \frac{1}{m_\alpha} \frac{FG_{\alpha_z}}{\nu_{\alpha_z \rightarrow D^+}}, \quad (25)$$

where

$$\nu_{\alpha_z \rightarrow D^+} = \frac{e^{5/2} \ln \Lambda}{6\sqrt{2}\pi^{3/2}\epsilon_0^2} \frac{n_{D^+} z^2}{(m_\alpha / \sqrt{m_r}) T_i^{3/2}} \quad (26)$$

is the Coulomb collision frequency of charge state α_z on the main D^+ ions. Here, $m_r = \frac{m_\alpha m_{D^+}}{m_\alpha + m_{D^+}}$ is the reduced mass, T_i

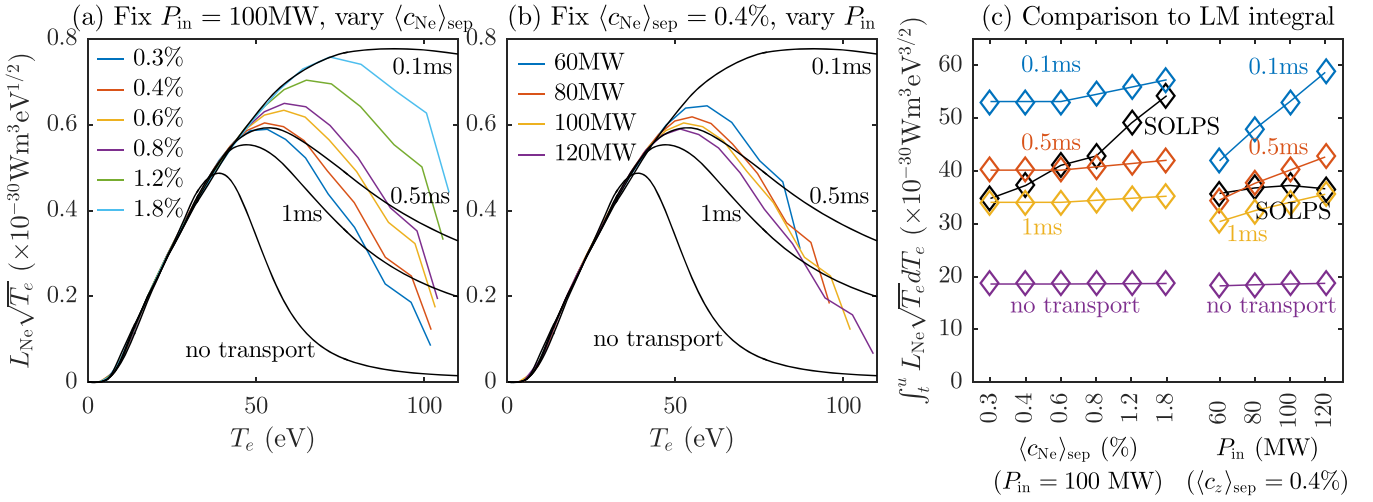


Figure 11. (a) and (b) The SOLPS electron cooling function due to neon (multiplied by $\sqrt{T_e}$; coloured lines) compared to fixed $n_e\tau$ calculations in black (labelled with their corresponding residence time τ , assuming $n_e = 1 \times 10^{20} \text{ m}^{-3}$). SOLPS values are plotted for the third SOL ring in the outer divertor at target ion flux rolover, for different values of $\langle c_{Ne} \rangle_{sep}$ and P_{in} , as labelled. (c) The integrals of the curves in (a) and (b).

has units of eV, and FG_{α_z} is the sum of the ion and electron temperature gradient forces, given in [35]:

$$FG_{\alpha_z} = e \left(\frac{z}{Z_{eff}} - 1 \right) z \left(2.2 \frac{\partial T_i}{\partial s} + 0.71 \frac{\partial T_e}{\partial s} \right) \quad (27)$$

(the coefficient 2.2 here comes from applying equation (20) in [36] to the specific case of neon). That is, aside from the main ion velocity, the parallel impurity ion velocity away from the target is set by a competition between the temperature gradient force (acting to increase $u_{\parallel\alpha_z}$) and Coulomb collisions with the main ions (acting to decrease $u_{\parallel\alpha_z}$).

The dashed lines in figure 13 show the right side of equation (25), demonstrating this approximation to be well met in these simulations for Ne^{7+} . In fact, this balance is also well met for the other main cooling charge states, which also have very similar parallel velocity profiles due to the weak z dependence in equation (25) for $z \gg 1$: $u_{\parallel\alpha_z} \propto 1/Z_{eff} - 1/z$ (at rolover, in the outer divertor third SOL ring, Z_{eff} varies weakly between 1.08 and 1.27 over the explored neon concentration range, so that $u_{\parallel\alpha_z} \propto 1/Z_{eff} - 1/z \sim 1 - 1/z$).

Furthermore, in these simulations the change (or lack of change) in impurity velocity is primarily a result of changes in the second term in equation (25), as plotted in figures 13(b) and (d) for Ne^{7+} . We can now understand why Ne^{7+} ions move to higher temperatures at higher $\langle c_{Ne} \rangle_{sep}$: at higher $\langle c_{Ne} \rangle_{sep}$ the rolover density is lower (recall figure 4(a)), so that the speed of Ne^{7+} ions away from the target is increased due to reduced collisions with D^+ ions (assuming relatively constant main ion velocity profiles, as is the case here). In contrast, for the P_{in} scan, the reduced rolover density at lower P_{in} does not cause an increase in $u_{\parallel\text{Ne}^{7+}}$ because it is offset by a concomitant reduction in the ion temperature.

Note finally that it is also now clear why the spreading out of the fractional abundances in figure 12 was most pronounced for the higher charge states: the largest differences in

$u_{\parallel\alpha_z}$ between the simulations occur in regions where the higher charge states are more abundant.

5.4. A predictive physics model for $n_e\tau$

What value of $n_e\tau$ should go into predictive calculations using the Lengyel model? For the comparison in figure 4 we used a constant fitted value of $n_e\tau = 0.5 \times 10^{20} \text{ m}^{-3} \text{ ms}$, but can our choice be based on a physics model, thus improving the predictive capability of the Lengyel model? One might argue from figure 6 that a more physical model for $n_e\tau$ (where $n_e\tau$ can vary) would not greatly improve the predictive capability of the Lengyel model beyond the $n_e\tau = \text{constant} = 0.5 \times 10^{20} \text{ m}^{-3} \text{ ms}$ ‘model’ used here. Indeed, for these ITER cases, where there is only a factor ~ 6 change in $n_e\tau$, this is a fair argument. However, when comparing cases with a larger variation in $n_e\tau$ it would be important (and more satisfactory from the perspective of physics understanding) to have a model for $n_e\tau$. Such a model is now considered.

In order to make progress, we assume that the electron density seen by the cooling impurities moving upstream can be approximated by the electron density at the divertor entrance. We then have

$$n_e\tau \approx n_{e,\text{div.ent.ring3}} \frac{L_{\parallel}}{\langle u_{\parallel\alpha_z,\text{cool}} \rangle} \quad (28)$$

where τ represents the time required for a cooling impurity to travel across an ion temperature gradient scale length, assumed here to be given by the parallel distance from target to outer divertor entrance L_{\parallel} , and

$$\langle u_{\parallel\alpha_z,\text{cool}} \rangle = \frac{1.68 \times 10^8}{\sqrt{m_r} \ln \Lambda} \frac{T_{iu}^{5/2}}{L_{\parallel} n_{e,\text{div.ent.ring3}}}, \quad (29)$$

is the average velocity of the main cooling charge states up the leg (away from the target). In (29), we have used equation (25)

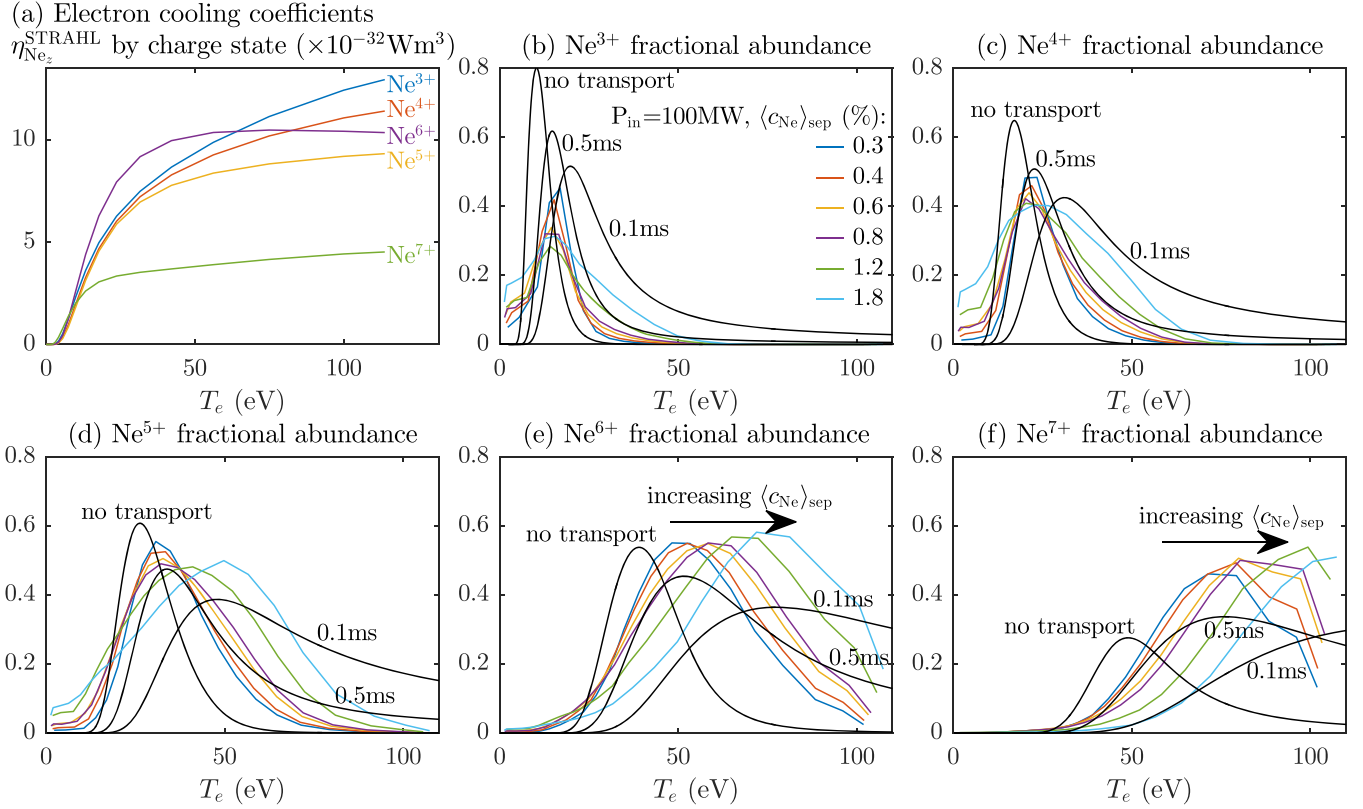


Figure 12. Composition of the SOLPS electron cooling functions shown in figure 11(a). (a) The electron loss coefficients from STRAHL for the main cooling charge states. (b)–(f) The simulated fractional abundances for those charge states [coloured according to the legend in (b)], compared to the three fixed residence time calculations in black, as labelled.

with several simplifying assumptions: (i) the main ion velocity u_{D^+} is assumed to be small; (ii) $T_i = T_e$; (iii) $\partial T_i / \partial s = T_{iu} / L_{\parallel}$; (iv) the cooling charge states have sufficiently high z that the z dependence in $u_{\parallel \alpha z}$ can be dropped; (v) Z_{eff} is close to the unity. Assuming further sufficient equipartition that T_{iu} scales like the standard two point model prediction for T_{eu} , and inserting (29) into (28), we obtain

$$n_e \tau \approx \alpha_{\text{fit}} \frac{\sqrt{m_r} \ln \Lambda \langle \kappa_{e||0,FL} \rangle^{5/7}}{4.11 \times 10^8} L_{\parallel}^{9/7} \frac{n_{e,\text{div.ent.ring3}}^2}{q_{\parallel u}^{5/7}}, \quad (30)$$

where α_{fit} is a fitting coefficient (expected to be of order unity) to account for the significant approximations made in the model.

In figure 14, we have plotted on the y-axis the values of $n_e \tau$ that give the best match between $L_{\text{Ne}}^{\text{SOLPS}} \sqrt{T_e}$ (from the simulations, solving for impurity transport of each charge state) and $L_{\text{Ne}}^{n_e \tau} \sqrt{T_e}$ (from the ADAS ionisation balance calculations assuming a single fitted $n_e \tau$ parameter). Note that the values for *all* simulations, not just at rollover, are shown. These fitted $n_e \tau$ values are plotted as a function of the physical model given by equation (30). Simulations within the $\langle c_{\text{Ne}} \rangle_{\text{sep}}$ scan are shown as black dots, while simulations within the P_{in} scan are shown as open circles. The best fit value for α_{fit} was found to be 0.90. It is quite striking that such a simple model as equation (30) can fit the simulation data so well. We now have a physics-based model for $n_e \tau$ and recommend the application

of equation (30) when using the Lengyel model for predictive purposes (at least in cases where the assumptions outlined above are reasonable).

We also have a physics reason why, as shown in figure 14, the range in fitted $n_e \tau$ is a factor ~ 2 larger for the $\langle c_{\text{Ne}} \rangle_{\text{sep}}$ scan than for the P_{in} scan. With increasing $\langle c_{\text{Ne}} \rangle_{\text{sep}}$, the upstream density decreases by a factor ~ 2.5 , while the upstream temperature remains similar. This reduced density means fewer collisions between impurity ions and D^+ ions (slowing the impurity ions) as well as fewer collisions between impurity ions and electrons (ionising them). This allows the temperature gradient forces (which remain similar) to push the impurity ions further upstream, reducing $n_e \tau$. A similar drop in upstream density also occurs as P_{in} is reduced in the P_{in} scan. However, this drop in upstream density is now concomitant with a drop in the upstream temperature, so that the temperature gradient forces are reduced. This opposes the drop in density so that $n_e \tau$ does not decrease by as much as in the $\langle c_{\text{Ne}} \rangle_{\text{sep}}$ scan.

There is an important caveat to note from this analysis. As already stated, these simulations used neon rates from the STRAHL database. These rates are calculated under the coronal approximation, where the electron density is assumed to be low enough that excited states decay radiatively before electron impact de-excitation can take place. At the densities of interest, more accurate rates such as those from ADAS 96 (derived from a collisional-radiative model) do not give

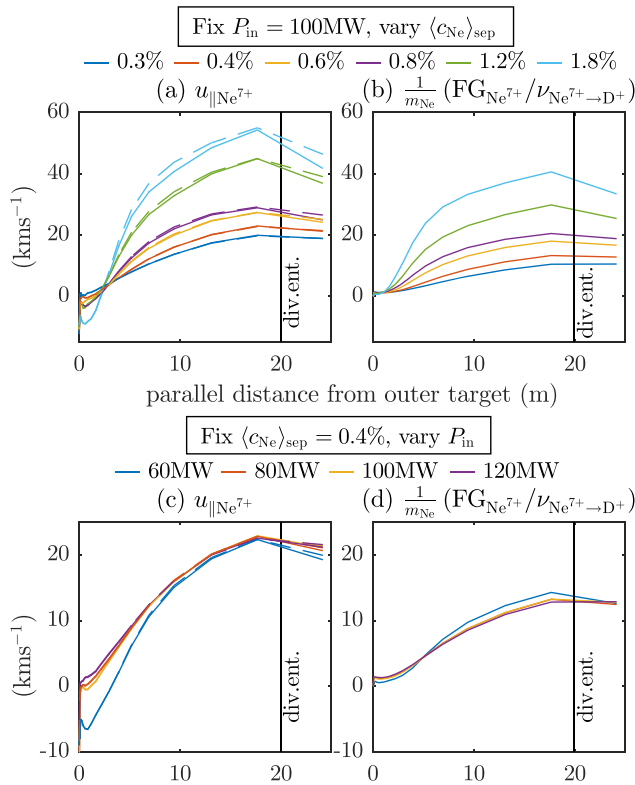


Figure 13. (a) Parallel velocities of Ne^{7+} for the fixed P_{in} , variable $\langle c_{\text{Ne}} \rangle_{\text{sep}}$ simulations. Also shown as dashed lines are the parallel velocities assuming that friction and thermal forces balance (right side of equation (25)). (b) The component of $u_{\parallel\alpha_z}$ due to the competition between the temperature gradient force (increasing $u_{\parallel\alpha_z}$) and Coulomb collisions with main ions (decreasing $u_{\parallel\alpha_z}$). (c) and (d) Same plots for the fixed $\langle c_{\text{Ne}} \rangle_{\text{sep}}$, variable P_{in} simulations.

such a pronounced drop in the electron cooling coefficients from Ne^{6+} to Ne^{7+} , as was seen in figure 12(a). Importantly, we do not expect the accuracy of equation (30) to be strongly affected by these more accurate rates, however differences in the values of $L_{\text{Ne}}^{n_e\tau} \sqrt{T_e}$ for a given $n_e\tau$ can be significant. These differences motivate us to self-consistently reconverge these simulations with ADAS 96 neon rates in future.

6. Neon enrichment

As noted in section 2.1, the Lengyel model predicts the impurity concentration in a particular flux ring in the outer divertor, whereas the relevant quantity for core performance is the impurity concentration in the upstream portion of the SOL neighbouring closed field lines. Here, we define the outer divertor neon enrichment η_{Ne} to be the ratio of these quantities:

$$\eta_{\text{Ne}} \equiv \frac{\langle c_{\text{Ne}} \rangle_{\text{div}}}{\langle c_{\text{Ne}} \rangle_{\text{sep}}} \quad (31)$$

It is important that $\langle c_{\text{Ne}} \rangle_{\text{div}}$ be taken in the third and not the first SOL ring of the outer divertor, so that η_{Ne} expresses our ability to enhance the neon concentration in regions where we want it (i.e. in the operationally limiting flux ring of the outer

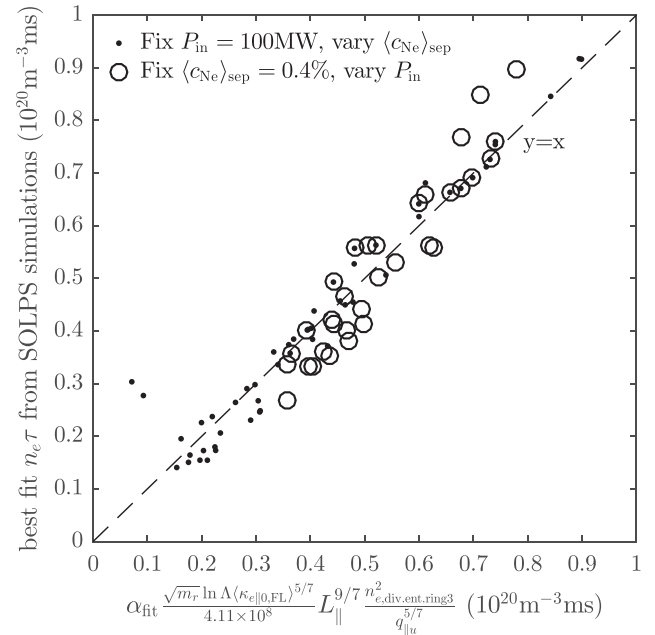


Figure 14. Comparison between the best fit $n_e\tau$ values from all SOLPS simulations in the database (y-axis) and the simplified physics model given by equation (30) (x-axis). Here, $\alpha_{\text{fit}} = 0.90$.

divertor), relative to regions where we do not want it (i.e. next to closed field lines in the main SOL).

In figure 15 we plot $\langle c_{\text{Ne}} \rangle_{\text{sep}}$ as a function of $\langle c_{\text{Ne}} \rangle_{\text{div}}$, for the entire database. Each puff scan is shown in its pre-rollover (dots), rollover (diamonds) and post-rollover (open circles) phases. A very interesting trend is observed for all puff scans, whereby the outer divertor neon enrichment increases as a function of the puff strength, i.e. as the degree of detachment increases. Note that, as shown in figure 15(b), this is a result of impurities becoming more compressed in the outer divertor, rather than electrons becoming more depleted. In figure 15(b) we plot the average neon density (all charge states) in the first SOL ring above the x-point, $\langle n_{\text{Ne}} \rangle_{\text{sep}}$, as a function of the average neon density in the third SOL ring of the outer divertor, $\langle n_{\text{Ne}} \rangle_{\text{div}}$. A similar trend is observed for the neon compression, $\langle n_{\text{Ne}} \rangle_{\text{div}} / \langle n_{\text{Ne}} \rangle_{\text{sep}}$, as for the enrichment, i.e. the compression increases with increasing puff. Note that, at rollover, both the enrichment and compression are fairly constant at $0.5 (\sim \pm 0.1)$ and $1.3 (\sim \pm 0.25)$, respectively.

This increasing compression of neon in the outer divertor with puffing can be seen in more detail by considering poloidal profiles along the entire third SOL ring, from inner to outer target. These are shown for both the neon concentration and density in figures 15(c) and (d). We see that there is a clear movement of neon from the inner to the outer divertor as the puffing rate is increased. Analysis is underway to try to explain this behaviour on the basis of a balancing of friction and thermal forces on the neon ions, combined with qualitative changes in the background ion flow. It is currently unclear whether the presence of drifts will change the qualitative trend shown in figure 15, though individual simulations do indicate a significant effect of drifts on the neon poloidal density profile [37]. A simplified consideration of the impact

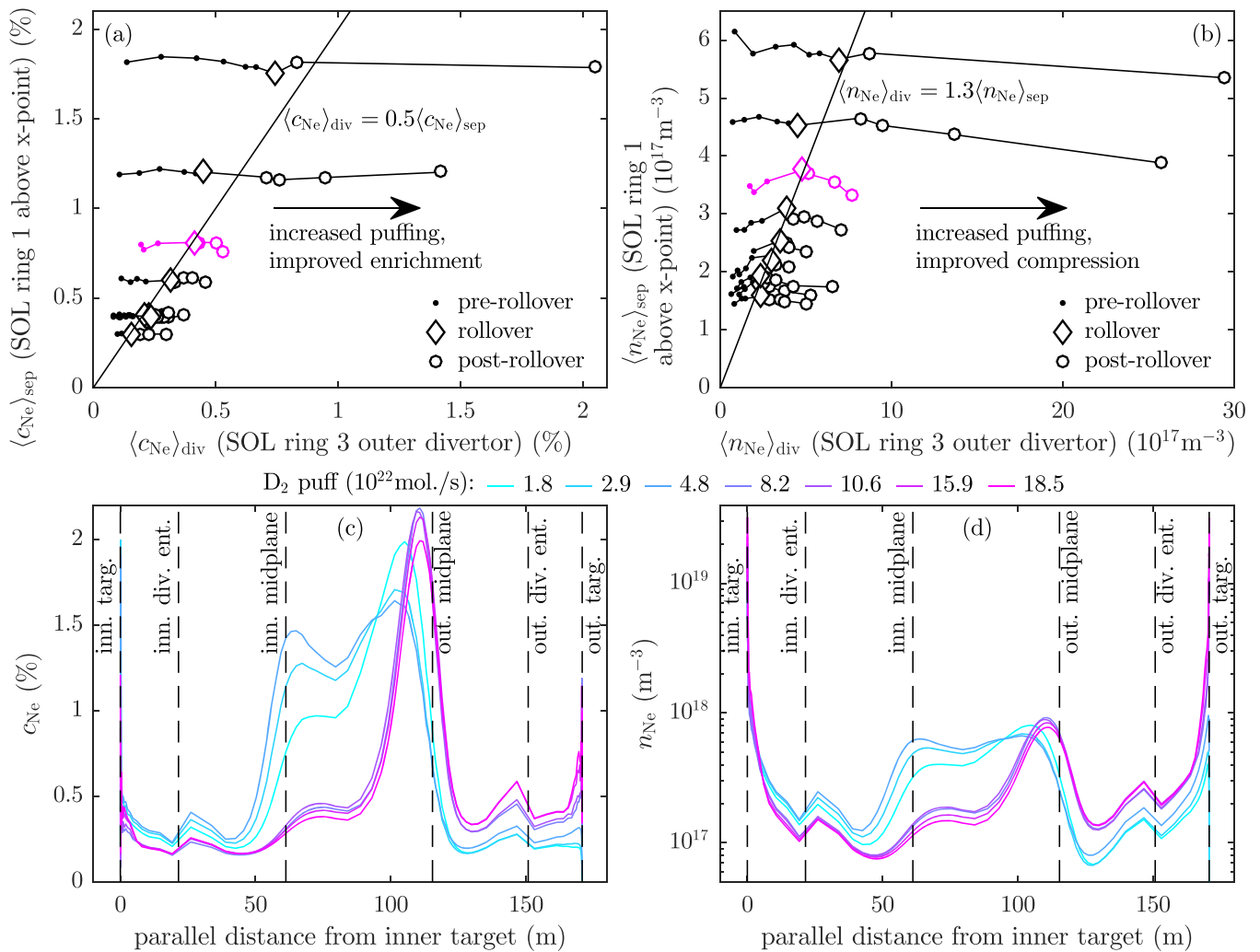


Figure 15. Increased enrichment and compression of neon in the outer divertor with increasing puff rate. (a) $\langle c_{\text{Ne}} \rangle_{\text{sep}}$ as a function of $\langle c_{\text{Ne}} \rangle_{\text{div}}$, for the entire database. We define the ratio of these quantities to be the enrichment, η_{Ne} . (b) $\langle n_{\text{Ne}} \rangle_{\text{sep}}$ as a function of $\langle n_{\text{Ne}} \rangle_{\text{div}}$. The ratio of these is the compression. Note that in (a) and (b) the straight lines indicate that at rollover both the enrichment and the compression are approximately constant, but as the puffing rate is increased the enrichment in the outer divertor improves. (c), (d) The concentrations and total density profiles of neon in the entire third SOL ring, from inner to outer targets, with increasing D_2 puff rate. These cases correspond to the $P_{\text{in}} = 100 \text{ MW}$, $\langle c_{\text{Ne}} \rangle_{\text{sep}} = 0.8\%$ puffing scan highlighted in magenta in (a) and (b).

of drifts on the Lengyel model prediction is presented in A. Note also that, for all these simulations the D_2 and Ne puffs were located at the top of the machine; it remains to be seen whether the behaviour shown in figure 15 is affected by these puffing locations.

What does all of this mean for the Lengyel model's ability to predict operationally relevant concentrations on the separatrix, as a function of operationally relevant electron densities on the separatrix? Figure 16 shows the simulated $\langle c_{\text{Ne}} \rangle_{\text{sep}}$ as a function of $\langle n_e \rangle_{\text{sep}}$. Also plotted in red are the simplified Lengyel model calculations using the same inputs as in section 2.3, except that now $n_{\text{eu}} = \langle n_e \rangle_{\text{sep}}$ (note that we keep the $q_{\parallel \text{u}}$ input to the Lengyel model as the value at the third SOL ring outer divertor entrance). Figure 16 should be compared to figure 4(a), which showed $\langle c_{\text{Ne}} \rangle_{\text{div}}$ in the third SOL ring as a function of $n_{\text{ediv.ent.ring3}}$.

Recall from figure 3 the relationship $\langle n_e \rangle_{\text{sep}} \approx 0.80 n_{\text{ediv.ent.ring3}}$ for all simulations in the database. This,

combined with $\langle c_{\text{Ne}} \rangle_{\text{sep}} \approx \langle c_{\text{Ne}} \rangle_{\text{div}}$ at rollover (figure 15), means that the agreement with the simplified Lengyel model scaling at rollover is similar to before, but with a slightly improved factor $\sim 4.3/0.8^2/2 = 3.4$ difference in the absolute predicted and simulated concentrations.

Importantly, however, the simulated behaviour after rollover is not captured by the model. In the simulations, $\langle n_e \rangle_{\text{sep}}$ decreases with increased puffing after rollover, while $\langle c_{\text{Ne}} \rangle_{\text{sep}}$ is kept constant. The Lengyel model would predict an increased concentration for this decreased upstream density and indeed, as was seen in figure 4(a), this is the case for the $\langle c_{\text{Ne}} \rangle_{\text{div}}$. However, because the enrichment is also improving, this increased $\langle c_{\text{Ne}} \rangle_{\text{div}}$ does not come at the expense of an increased $\langle c_{\text{Ne}} \rangle_{\text{sep}}$. This potentially has important consequences for power handling, since more operationally favourable conditions that are still tolerable from an exhaust point of view might be accessed by simply puffing more to improve impurity enrichment in the outer divertor. Note,

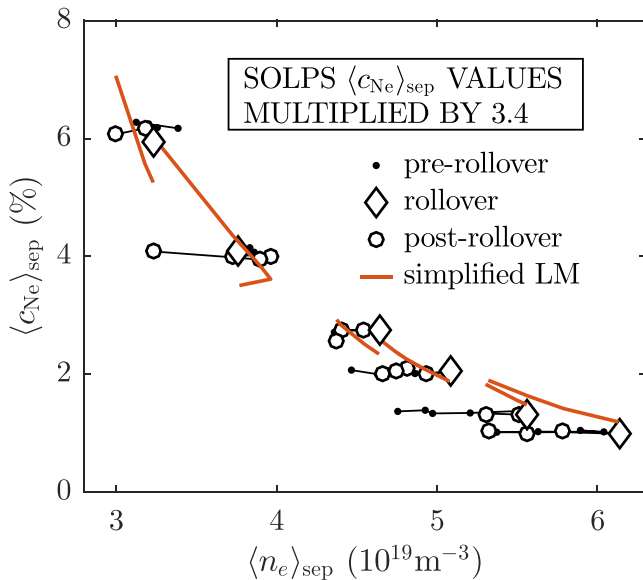


Figure 16. Ability of the simplified Lengyel model to predict operationally relevant upstream impurity concentrations $\langle c_{\text{Ne}} \rangle_{\text{sep}}$ as a function of operationally relevant upstream densities $\langle n_e \rangle_{\text{sep}}$. This figure should be compared to figure 4(a). The simplified Lengyel model calculations are also shown, using $\langle n_e \rangle_{\text{sep}}$ as input.

however, that it is unlikely this trend can continue forever. At some point either an MARFE will form risking H-mode access, or the inner divertor will be so starved of neon that it becomes the operationally limiting divertor. Future work will explore more strongly detached simulations than those available within this database.

7. Conclusions

Before drawing conclusions from this work, it is important to be clear about the conclusions we *cannot* draw. We cannot conclude much regarding the *general* applicability of the Lengyel models (except for the prediction of $n_e \tau$ for impurities, discussed below). This is because of potentially important physics that we know to be missing from the simulations (for example drifts and turbulence), as well as the limited parameter space which they cover (relative to all tokamaks, past, present, and future). Such generality can only be assessed through further simulations including more physics, as well as experimental measurement. Regarding the assessment via simulation, an important outcome of this work is the analysis procedure, i.e. the progressive simplification of equation (19), that we have used to understand the dominant physics causing variation from the simplified Lengyel model. This procedure should be generally transferrable to other codes applied to other machines.

Despite this strong proviso, we can still draw important and useful conclusions regarding the application of the Lengyel models to ITER, assuming the SOLPS-4.3 physics model. These are as follows:

- For SOLPS-4.3 simulations of ITER baseline neon seeded plasmas, in a divertor flux tube that is operationally limiting, the ‘simplified’ Lengyel model tends to overpredict the simulated impurity concentration at target ion

flux rollover by a factor 4.3 (both ‘simplified’ and ‘full’ Lengyel models, as described in section 1, give very similar results, within $\sim 14\%$ of each other).

- Despite this factor ~ 4.3 overprediction of the required divertor neon concentration, the Lengyel models predict remarkably well the *scaling* of the interdependencies between upstream density, outer divertor impurity concentration and upstream parallel energy flux density, at target ion flux rollover. Interestingly, even after target ion flux rollover, the Lengyel model continues to predict the increased *divertor* impurity concentration as the upstream density decreases (though not the *upstream* impurity concentration since the impurity enrichment increases in the outer divertor as the puffing is increased). The outer divertor impurity compression increases in a way that is consistent with the decreased upstream density and with the Lengyel models.
- Approximately half of the observed factor ~ 4.3 difference can be explained by additional energy losses besides neon cooling and additional energy fluxes besides electron conduction, neither of which are accounted for in the Lengyel models. Radial transport losses from the considered flux tube are at least as important in these simulations as deuterium neutral losses (the latter decrease in importance at higher neon concentrations). We expect deuterium neutral losses to become more important at lower impurity concentrations and/or with increased neutral trapping.
- A further factor ~ 1.5 difference is accounted for by the incorrect assumption in the Lengyel models that electron static pressure is constant from the divertor entrance to the radiating region. Although total (electron plus ion) static pressure is approximately constant in the simulations, the ratio T_i/T_e changes significantly, so that a factor ~ 1.5 increase in the calculated concentration is incurred by the assumption of constant electron static pressure.
- Of all the Lengyel model assumptions, the one that most affects the predicted scaling of divertor neon concentration with upstream density, compared to the simulations, is the assumption of constant $n_e \tau$ for the calculation of the electron cooling function due to neon. In the simulations, the impurity residence time is not constant. It increases with increasing upstream density (due to increased friction with main ions) and with decreasing upstream ion temperature (due to decreased ion temperature gradient force). At low density this acts to push upstream the inefficiently-radiating, high charge state impurities, thus reducing the required impurity concentration. A physics-based model has been derived for $n_e \tau$, given by equation (30).
- In these simulations, this effect of changing $n_e \tau$ does not worsen the overall scaling of divertor impurity concentration with upstream density compared to the Lengyel model. It is cancelled out by an accumulation of other physics included in the simulations: the aforementioned energy loss and flux channels, the poloidally non-constant

electron pressure and neon concentration, and the non-constant magnetic field strength. On their own, none of these cause a significant deviation from the simplified Lengyel model, but when combined they are sufficient to cancel the effect of changing $n_e\tau$.

- Neon is found to migrate from the inner divertor to the outer divertor as the puffing rate, and thereby the degree of detachment, is increased. As a result, the outer divertor neon enrichment increases in these drift-free simulations. Future work will aim to understand this behaviour and whether it is still observed in the presence of drifts.
- Although the outer divertor neon enrichment increases with puffing, it is approximately constant at target ion flux rollover, with a value of ~ 0.5 for all upstream concentrations. In addition, the average separatrix electron density increases approximately linearly with the electron density at the divertor entrance in the operationally-limiting flux tube. As a result, the Lengyel model still accurately predicts the scaling dependency between the operationally relevant upstream $\langle c_{\text{Ne}} \rangle_{\text{sep}}$ and $\langle n_e \rangle_{\text{sep}}$ at rollover.
- As a result of improved neon enrichment beyond rollover, more operationally advantageous upstream conditions with lower electron density can be accessed in these strongly detached simulations, without adversely affecting plasma exhaust. Even more strongly detached simulations are required in order to assess how far this advantage can be pushed.

Acknowledgments

The authors would like to thank Bruce Lipschultz for his keen insights and useful suggestions. This work was conducted under the auspices of the ITER Scientist Fellow Network. It has been funded by the RCUK Energy Programme (Grant No. EP/T012250/1). To obtain further information on the data and models underlying this paper please contact PublicationsManager@ukaea.uk. The views and opinions expressed herein do not necessarily reflect those of the ITER organisation.

Appendix A. A simplified consideration of drifts

Here, we consider a simple modification of the Lengyel model to allow a rough estimate of how convective drifts might affect the required impurity concentration for detachment onset. Consider the strongly simplified case where a constant fraction f_{conv} of the parallel energy flux density is carried by convection due to drifts, i.e.

$$q_{\parallel\text{conv}} = f_{\text{conv}} q_{\parallel}, \quad (32)$$

throughout the SOL. We substitute (31) into (2) and use $T_{\text{eu}} = (1 - f_{\text{conv}})^{2/7} T_{\text{eu}}^{\text{2PM}}$, while keeping all other assumptions the same. We find that

$$c_{\alpha} = (1 - f_{\text{conv}})^{(3-2\beta)/7} c_{\alpha}^{\text{LM,simp}}, \quad (33)$$

where $c_{\alpha}^{\text{LM,simp}}$ is the original simplified Lengyel model expression for the required impurity concentration given by

equation (17). In equation (32), β represents the degree to which the integral $L_{\text{INT}} = \int_0^u L_{\alpha}^{n_e\tau} \sqrt{T_e} dT_e$ depends on T_{eu} :

$$L_{\text{INT}} \propto T_{\text{eu}}^{\beta}. \quad (34)$$

This dependence is given in figures 2 and 3 of [12]. Depending on $n_e\tau$ and on the seeded impurity, β lies approximately between 0 and 1. We conclude from equation (32) that, in this very specific case where drifts are assumed to result in a constant convective fraction, their effect on the required impurity concentration is small.

There are several provisos to the weak dependence between c_{α} and f_{conv} given by equation (32):

- Even this weak dependence can become important if f_{conv} is sufficiently close to one. Indeed, this appears to be the case for the recently published simulations of DIII-D [38]. The authors report values of $f_{\text{conv}} \approx 0.995$ at detachment in the presence of drifts, moving the SOL profiles significantly away from those predicted by the Lengyel model. However, recent simulations of ITER equivalent to those reported here, but with drifts turned on, do not have such large values of f_{conv} [37]. As can be seen from figure 11 of that publication, for cases near the ion target flux rollover, the poloidal energy flow towards the outer target is weakly affected by the presence of drifts, implying a relatively small f_{conv} for ITER, compared to DIII-D¹⁶.
- Equation (32) does not consider how drifts might affect the total $q_{\parallel\text{u}}$ entering the divertor. Here, we treat $q_{\parallel\text{u}}$ as an input parameter to the Lengyel model, but it must be borne in mind that the relationship between the ‘true’ input parameter P_{in} and the Lengyel model input parameter $q_{\parallel\text{u}}$ will be affected by drifts; for a given P_{in} , drifts will alter the proportion of power entering the outer divertor compared to the inner.
- Changes in the impurity compression in the divertor due to drifts are not considered here.
- Finally, we note that a stronger dependence on the convective fraction could be found for instances where that fraction is not assumed constant.

A proper understanding of how drifts might affect the Lengyel scalings reported in this paper will therefore require a similarly sized database to the one assessed here, but with drifts turned on.

Appendix B. The pre-rollover phase

The primary focus of this paper has been on how well the simplified Lengyel model predicts the $(c_{\text{Ne}}, q_{\parallel\text{u}}, n_{\text{eu}})$ values required for the target ion flux density to roll over. This focus was motivated by the expectation that rollover will be required to manage heat loads in the ITER $Q = 10$ baseline scenario, as well as in future reactors. Nevertheless, for current machines, as well as for ITER’s pre-fusion power operation phase, it is

¹⁶ Additional indications of the importance of drifts on TCV and DIII-D were recently reported in [39, 40].

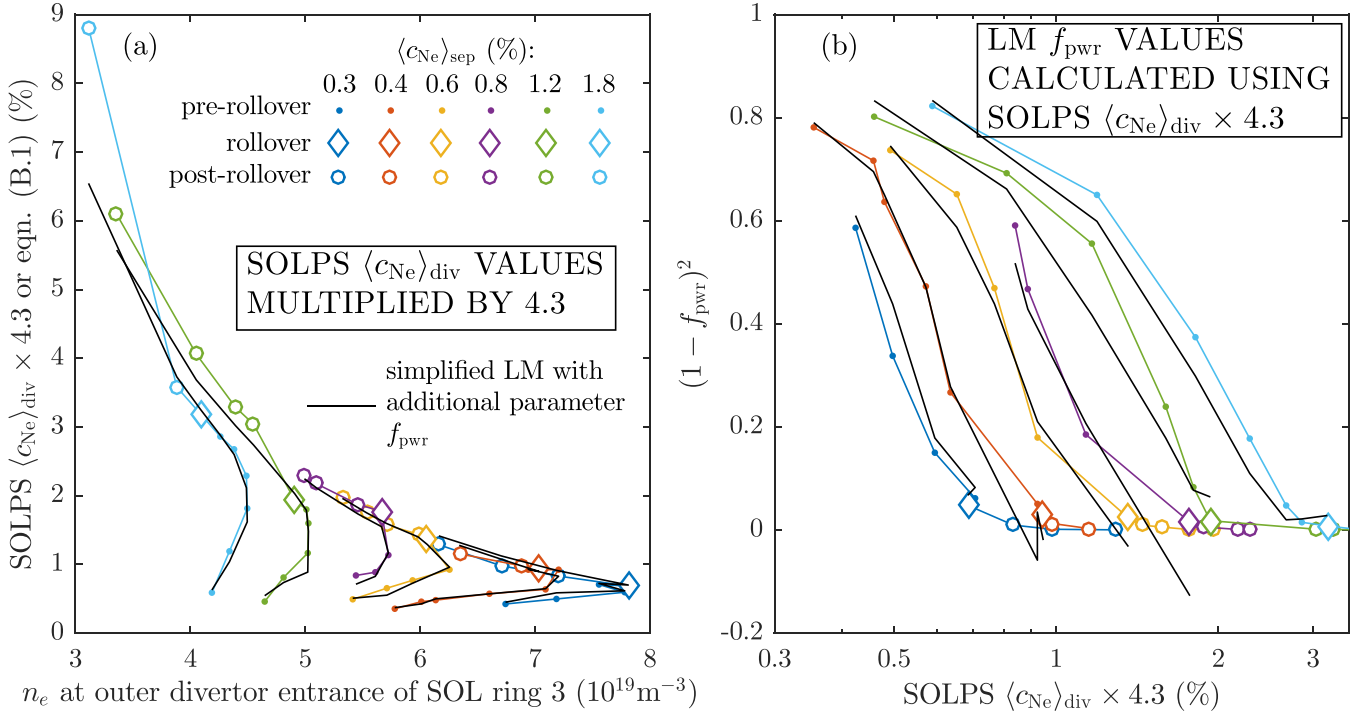


Figure 17. (a) Identical to figure 4(a), but now comparing the simulation results to the pre-rollover phase as well, using equation (34). (b) $(1 - f_{pwr})^2$ as a function of the simulated $\langle c_{Ne} \rangle_{div} \times 4.3$, for the same simulations in (a). Black lines show the predictions from equation (34) for the pre-rollover phase, using the simulated $\langle c_{Ne} \rangle_{div} \times 4.3$ as input.

interesting to consider how such a simple model performs in the lead up to rollover.

To assess this, we must introduce an extra parameter to the simplified Lengyel model given by equation (17). Before rollover, $q_{||t} = 0$ is no longer a valid assumption. We therefore include the dissipated power fraction in the flux ring of interest, $f_{pwr} = 1 - q_{||t}/q_{||u}$. Keeping all of the other simplified Lengyel model assumptions, equation (17) becomes

$$c_{\alpha} = \frac{q_{||u}^2 \left(1 - (1 - f_{pwr})^2\right)}{2\kappa_{e||0,FL} n_{cu}^2 (T_{cu}^{2PM})^2 \int_0^{T_{cu}^{2PM}} L_{\alpha}^{n_e \tau} \sqrt{T_e} dT_e}. \quad (36)$$

Note that we are still integrating from $T_e = 0$ in equation (34), i.e. the actual T_{et} is assumed to remain sufficiently small so that $\int_{T_{et}}^{T_{cu}^{2PM}} L_{\alpha}^{n_e \tau} \sqrt{T_e} dT_e \approx \int_0^{T_{cu}^{2PM}} L_{\alpha}^{n_e \tau} \sqrt{T_e} dT_e$.

Figure 17(a) shows the same plot as figure 4(a), but now with the solid black lines given by equation (34), rather than equation (17). In this case, we used the simulated values of f_{pwr} as additional inputs and compared to the entire simulated puff scan at each $\langle c_{Ne} \rangle_{sep}$, including the pre-rollover phase (shown as dots). As previously, the simulated $\langle c_{Ne} \rangle_{div}$ were multiplied by a factor 4.3 to obtain a good comparison.

For simulations at (and beyond) rollover, we have that $f_{pwr} \approx 1$. The concentrations predicted by equations (17) and (34) are therefore very similar in this phase, giving the same agreement with SOLPS-4.3 shown previously in figure 4(a). Now, with the addition of the f_{pwr} parameter taken from the simulations, we find an excellent

agreement in the pre-rollover phase as well. That is, by specifying $q_{||u}$ and $n_{e,div.ent.ring3}$ from the simulations, equation (34) predicts well the neon concentration required in the divertor to achieve a given f_{pwr} , after multiplication by a constant factor 1/4.3, in attached and detached phases. This implies that equation (34) can also be used to predict the simulated f_{pwr} for a given $(\langle c_{Ne} \rangle_{div}, q_{||u}, n_{e,div.ent.ring3})$, once the simulated $\langle c_{Ne} \rangle_{div}$ has been multiplied by 4.3. Indeed, this is shown to be the case in figure 17(b), where we compare the simulated (coloured) and predicted (black) values of $(1 - f_{pwr})^2$ in the pre-rollover phase. Values are plotted as a function of the simulated $\langle c_{Ne} \rangle_{div} \times 4.3$ for the same simulations shown in figure 17(a).

References

- [1] Lengyel L. 1981 *Analysis of Radiating Plasma Boundary Layers* (Munich: : Max-Planck-Institut für Plasmaphysik)
- [2] Lackner K. and Schneider R. 1993 The role of edge physics and confinement issues in the fusion reactor *Fusion Technology 1992* ed C Ferro, M Gasparotto and H Knoepfel (Amsterdam: North-Holland) pp 107–16
- [3] Hutchinson I.H. 1994 Thermal front analysis of detached divertors and MARFES *Nucl. Fusion* **34** 1337–48
- [4] Post D., Abdallah J., Clark R.E.H. and Putvinskaya N. 1995 Calculations of energy losses due to atomic processes in tokamaks with applications to the international thermonuclear experimental reactor divertor *Phys. Plasmas* **2** 2328–36
- [5] Mandrekas J., Stacey W.M. and Kelly F. 1996 Impurity seeded radiative power exhaust solutions for ITER *Nucl. Fusion* **36** 917–26

- [6] Pitcher C.S. and Stangeby P.C. 1997 Experimental divertor physics *Plasma Phys. Control. Fusion* **39** 779–930
- [7] Wenzel U., Carlson A., Fuchs C., Kastelewicz H. and Napiontek B. 1999 Spectroscopic study of the radiation in divertor I of ASDEX upgrade at high density *Plasma Phys. Control. Fusion* **41** 801–18
- [8] Schneider R., Bonnin X., Borrass K., Coster D.P., Kastelewicz H., Reiter D. *et al* 2006 Plasma edge physics with B2-eirene *Contrib. Plasma Phys.* **46** 3–191
- [9] Kallenbach A. *et al* 2013 Impurity seeding for tokamak power exhaust: from present devices via ITER to DEMO *Plasma Phys. Control. Fusion* **55** 124041
- [10] Siccino M., Fable E., Lackner K., Scarabosio A., Wenninger R.P. and Zohm H. 2016 A 0D stationary model for the evaluation of the degree of detachment on the divertor plates *Plasma Phys. Control. Fusion* **58** 125011
- [11] Lipschultz B., Parra F.I. and Hutchinson I.H. 2016 Sensitivity of detachment extent to magnetic configuration and external parameters *Nucl. Fusion* **56** 056007
- [12] Reinke M.L. 2017 Heat flux mitigation by impurity seeding in high-field tokamaks *Nucl. Fusion* **57** 034004
- [13] Goldston R.J., Reinke M.L. and Schwartz J.A. 2017 A new scaling for divertor detachment *Plasma Phys. Control. Fusion* **59** 055015
- [14] Pacher H.D., Kukushkin A.S., Pacher G.W., Kotov V., Pitts R.A. and Reiter D. 2015 Impurity seeding in ITER DT plasmas in a carbon-free environment *J. Nucl. Mater.* **463** 591–5
- [15] Pitts R.A. *et al* 2019 Physics basis for the first ITER tungsten divertor *Nucl. Mater. Energy* **20** 100696
- [16] Behringer K. 1987 *Description of the Impurity Code STRAHL* (Culham: JET Joint Undertaking)
- [17] Carolan P.G. and Piotrowicz V.A. 1983 The behaviour of impurities out of coronal equilibrium *Plasma Phys.* **25** 1065–86
- [18] Stangeby P.C. 2000 *The Plasma Boundary of Magnetic Fusion Devices* (London: Taylor and Francis)
- [19] Park J.-S., Bonnin X. and Pitts R. 2021 Assessment of ITER divertor performance during early operation phases *Nucl. Fusion* **61** 016021
- [20] Aho-Mantila L. *et al* 2017 Assessment of SOLPS5.0 divertor solutions with drifts and currents against L-mode experiments in ASDEX upgrade and JET *Plasma Phys. Control. Fusion* **59** 035003
- [21] Moulton D., Corrigan G., Harrison J.R. and Lipschultz B. 2018 Neutral pathways and heat flux widths in vertical- and horizontal-target EDGE2D-EIRENE simulations of JET *Nucl. Fusion* **58** 096029
- [22] Lipschultz T. *et al* 2013 Scaling of the tokamak near the scrape-off layer H-mode power width and implications for ITER *Nucl. Fusion* **53** 093031
- [23] Braams B.J. 1986 Computational studies in tokamak equilibrium and transport *PhD Thesis* University of Utrecht
- [24] Valanju P.M., Kotschenreuther M., Mahajan S.M. and Canik J. 2009 Super-X divertors and high power density fusion devices *Phys. Plasmas* **16** 056110
- [25] Loarte A. 2001 Effects of divertor geometry on tokamak plasmas *Plasma Phys. Control. Fusion* **43** R183–224
- [26] Fil A., Lipschultz B., Moulton D., Dudson B.D., Février O., Myatra O., Theiler C., Verhaegh K. and Wensing M. 2020 Separating the roles of magnetic topology and neutral trapping in modifying the detachment threshold for TCV *Plasma Phys. Control. Fusion* **62** 035008
- [27] Casali L., Sang C., Moser A.L., Covele B.M., Guo H.Y. and Samuell C. 2018 Modelling the effect of divertor closure on detachment onset in DIII-D with the SOLPS code *Contrib. Plasma Phys.* **58** 725–31
- [28] Moser A.L., Casali L., Covele B.M., Leonard A.W., McLean A.G., Shafer M.W., Wang H.Q. and Watkins J.G. 2020 Separating divertor closure effects on divertor detachment and pedestal shape in DIII-D *Phys. Plasmas* **27** 032506
- [29] Casali L., Eldon D., Boedo J.A., Leonard T. and Covele B. 2020 Neutral leakage, power dissipation and pedestal fueling in open vs closed divertors *Nucl. Fusion* **60** 076011
- [30] Sang C., Guo H.Y., Stangeby P.C., Lao L.L. and Taylor T.S. 2017 SOLPS analysis of neutral baffling for the design of a new diverter in DIII-D *Nucl. Fusion* **57** 056043
- [31] Guo H.Y. *et al* 2019 First experimental tests of a new small angle slot divertor on DIII-D *Nucl. Fusion* **59** 086054
- [32] Casali L., Covele B.M. and Guo H.Y. 2019 The effect of neutrals in the new SAS divertor at DIII-D as modelled by SOLPS *Nucl. Mater. Energy* **19** 537–43
- [33] Shafer M.W. *et al* 2019 Dependence of neutral pressure on detachment in the small angle slot divertor at DIII-D *Nucl. Mater. Energy* **19** 487–92
- [34] Senichenkov I.Y., Kaveeva E.G., Sytova E.A., Rozhansky V.A., Voskoboinikov S.P., Veselova I.Y., Coster D.P., Bonnin X. and Reimold F. 2019 On mechanisms of impurity leakage and retention in the tokamak divertor *Plasma Phys. Control. Fusion* **61** 045013
- [35] Bergmann A., Igitkhanov Y., Braams B., Coster D.P. and Schneider R. 1996 Implementation into B2 of a 21-moment description for the parallel transport *Contrib. Plasma Phys.* **36** 192–6
- [36] Chapman S. 1958 Thermal diffusion in ionized gases *Proc. Phys. Soc.* **72** 353–62
- [37] Kaveeva E. *et al* 2020 SOLPS-ITER modelling of ITER edge plasma with drifts and currents *Nucl. Fusion* **60** 046019
- [38] Jaervinen A.E., Allen S.L., Leonard A.W., McLean A.G., Moser A.L., Rognien T.D. *et al* 2020 Role of poloidal EB drift in divertor heat transport in DIII-D *Contrib. Plasma Phys.* **60** e201900111
- [39] Wensing M., Loizu J., Reimerdes H., Duval B.P., Wischmeier M. and the TCV team 2020 X-point potential well formation in diverted tokamaks with unfavorable magnetic field direction *Nucl. Fusion* **60** 054005
- [40] Casali L., Osborne T.H., Grierson B.A., McLean A.G., Meier E.T., Ren J., Shafer M.W., Wang H. and Watkins J.G. 2020 Improved core-edge compatibility using impurity seeding in the small angle slot (SAS) divertor at DIII-D *Phys. Plasmas* **27** 062506